

Discontinuous Fluctuation Distribution

Matthew Hubbard

School of Computing, University of Leeds, Leeds, LS2 9JT, UK.

Abstract

This paper describes a new numerical scheme for the approximation of steady state solutions to systems of hyperbolic conservation laws. It generalises the fluctuation distribution framework by allowing the underlying representation of the solution to be discontinuous. This leads to edge-based fluctuations in addition to the standard cell-based fluctuations, which are then distributed to the cell vertices in an upwind manner which retains the properties of the continuous scheme (positivity, linearity preservation, conservation, compactness and continuity). Numerical results are presented on unstructured triangular meshes in two space dimensions for linear and nonlinear scalar equations as well as the Euler equations of gasdynamics. The accuracy of the approximation in smooth regions of the flow is shown to be very similar to the corresponding continuous scheme, but the discontinuous approach improves the sharpness with which discontinuities in the flow can be captured and provides additional flexibility which will allow adaptive techniques to be applied simply to improve efficiency.

Key words: Fluctuation Distribution, Hyperbolic Conservation Laws, Discontinuous Representation.

PACS: 65M99, 76M25

1 Introduction

The concept of fluctuation distribution was formalised 25 years ago [23] as a potential alternative to flux-based finite volume schemes for approximating hyperbolic conservation laws. It was built on previous work by Ni [18] and Sells [27], who placed the emphasis on using differences between fluxes, rather than the fluxes themselves, to predict the evolution of the flow. In one space dimension it was simple to reproduce the most valuable properties of the finite volume schemes, such as upwinding, positivity and conservation, and the

Email address: meh@comp.leeds.ac.uk (Matthew Hubbard).

schemes developed were easily extended to nonlinear systems using existing techniques [22]. The advantages of the fluctuation distribution approach become more apparent when simulating multidimensional problems, where the framework is far better able to incorporate genuinely multidimensional physical phenomena, avoiding the inherently one-dimensional concept of a Riemann solver which is typically retained when upwind flux-based algorithms are extended to higher dimensions.

Since their inception, fluctuation distribution schemes have been developed which provided genuinely multidimensional modelling which can achieve very high orders of accuracy without spurious oscillations for both steady state and time-dependent scalar equations, along with generalisations to nonlinear systems of conservation laws. Details of both their foundations and some of the most important recent developments can be found in the reviews presented in [2,30] and the references therein. However, the work presented in this paper is primarily concerned with a new strand of research which builds on the fundamental components of fluctuation distribution:

- an upwind scheme for simulating scalar advection (most naturally on unstructured meshes of simplices) which can also cope with the presence of non-homogeneous terms [25,28];
- a conservative linearisation for nonlinear equations and systems (which isn't essential but greatly aids in the retention of desired properties when extending scalar schemes to nonlinear systems of equations) [11];
- a generalisation of the scalar scheme to systems of equations, typically carried out through either wave decomposition models [17,19,26] or matrix distribution schemes [29].

The more recent developments in high order and time-dependent schemes may be applied in the new framework, but this is the subject of future research and will only be discussed briefly at the end of this paper.

The finite volume approach remains an extremely popular choice for simulating flows of realistic complexity, largely due to its ability to provide plausible solutions in the most demanding of situations. Although fluctuation distribution does not yet provide the same level of robustness, particularly in three dimensions, it has the advantage that when it does provide a sensible solution, it is typically far more accurate, due to its more realistic representation of multidimensional flow physics.

More recently, the discontinuous Galerkin approach (see, for example [8,30] for an overview) has emerged as a strong challenger to finite volumes. In fact it can be viewed as a generalisation of the finite volume framework which retains the flux-based form at the mesh edges but also includes the effects of variations within each cell in the manner of a finite element (or fluctuation distribution)

scheme. Allowing the representation of the dependent variable to be discontinuous provides considerably more flexibility than continuous finite elements, especially in terms of applying upwinding and adaptive techniques. Formulating the approach as a non-conforming finite element scheme facilitates formal analysis that is not available to the finite volume approach. The success of these schemes suggests that there are significant benefits to be found in the combination of a discontinuous representation (for flexibility and shock capturing) with proper modelling of variations within mesh cells (for accuracy). In fact, the discontinuous Galerkin scheme has already been reformulated as a fluctuation distribution scheme [6], and then combined with a standard technique for obtaining high order accuracy from a first order positive scheme. The work in this paper will present a different form of discontinuous scheme, derived purely from a fluctuation distribution viewpoint.

Until now, fluctuation distribution has been based on a discrete solution that is constrained to be continuous over the computational domain. The purpose of the research presented here is to relax this constraint and examine the possibility of combining the fluctuation distribution approach with a discontinuous representation of the solution.

- The fluctuation distribution framework provides
 - schemes which have been designed to retain at a discrete level the most important underlying physical processes, retaining a genuinely multidimensional representation which flux-based schemes aren't capable of;
 - a framework in which it is simple to discretise source terms which represent processes having a natural balance with the fluxes [20,24] and retain equilibria inherent in the underlying equations;
 - genuinely multidimensional upwinding (and hence positivity).
- Allowing the scheme to use a discontinuous representation of the dependent variable provides, in addition,
 - a framework within which h - and p -adaptivity can be carried out simply;
 - a localised system which aids in the construction of high order schemes which are free of numerically induced oscillations.

Instead of taking the discontinuous Galerkin approach, which uses numerical fluxes to deal with the discontinuous representation, the new scheme retains the basic fluctuation distribution approach and applies it to additional, edge-based, fluctuations which arise due to the discontinuities. These are calculated at each mesh edge and then distributed using appropriate forms for the conservative linearisation, the decomposition of the linearised system and the distribution of the scalar components.

This paper will describe discontinuous fluctuation distribution in detail, as it is applied to both scalar hyperbolic conservation laws and nonlinear systems, on unstructured triangular meshes in two space dimensions. Only steady state

solutions and schemes based on a piecewise linear representation of the dependent variables will be considered. The most commonly used continuous fluctuation distribution schemes, which will be used here in the discontinuous scheme to distribute the contributions from the mesh cells, will be described in Sections 2 (scalar equations) and 3 (nonlinear systems of equations). The extension to allow for discontinuities in the solution across cell edges will be described in Section 4. The method is then applied to the scalar advection equation, a form of the inviscid Burgers' equation and the Euler equations of gasdynamics in Section 5, where results are provided for a range of two-dimensional test cases. The future development of the method is discussed in Section 6.

2 Fluctuation Distribution

Consider the scalar conservation law governing the evolution of an unknown quantity $u(\vec{x}, t)$ and given by

$$u_t + \vec{\nabla} \cdot \vec{f} = 0 \quad \text{or} \quad u_t + \vec{\lambda} \cdot \vec{\nabla} u = 0 \quad (1)$$

on a domain Ω , with appropriate initial conditions and Dirichlet boundary conditions imposed on the inflow part of the boundary $\partial\Omega$. Here \vec{f} represents the conservative flux vector and $\vec{\lambda} = \partial\vec{f}/\partial u$ defines the advection velocity associated with the conservation law (1). This equation has an associated fluctuation which, for a triangular mesh cell Δ (for simplicity, the two-dimensional case will be considered from now on), is given by

$$\phi = - \int_{\Delta} \vec{\lambda} \cdot \vec{\nabla} u \, d\Omega = - \int_{\Delta} \vec{\nabla} \cdot \vec{f} \, d\Omega = \oint_{\partial\Delta} \vec{f} \cdot \vec{n} \, d\Gamma, \quad (2)$$

in which \vec{n} represents the inward pointing unit normal to the cell boundary. When u is assumed to have a piecewise linear continuous representation with values stored at the mesh nodes, the discrete counterpart of ϕ is evaluated using an appropriate (conservative) linearisation [11,30]. Ideally, this allows the integration in Equation (2) to be carried out exactly with respect to the discrete representation of the flow variables, giving

$$\phi = -S_{\Delta} \tilde{\vec{\lambda}} \cdot \tilde{\vec{\nabla}} u = -\frac{1}{2} \sum_{i \in \Delta} u_i \tilde{\vec{\lambda}} \cdot \vec{n}_i = - \sum_{i \in \Delta} k_i u_i, \quad (3)$$

where S_{Δ} is the cell area and the symbol $\tilde{\sim}$ indicates an appropriately linearised quantity. The index i loops over the vertices of Δ and \vec{n}_i is the inward unit normal to the i^{th} edge (opposite the i^{th} vertex, see the left hand side of

Figure 1) multiplied by the length of that edge. The k_i are defined by

$$k_i = \frac{1}{2} \tilde{\lambda} \cdot \vec{n}_i \quad (4)$$

and represent “inflow parameters” which indicate the direction of flow through a cell edge ($k_i > 0$ represents inflow through the edge opposite vertex i , while $k_i < 0$ represents outflow). Note that a piecewise linear representation of the solution within each mesh cell will be assumed throughout this work, with the extension to higher degree polynomials considered in future research.

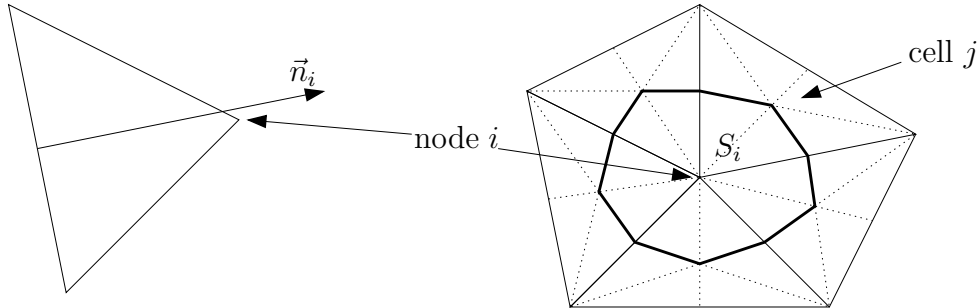


Fig. 1. The geometry of an individual mesh cell and its edge normal (left) and the median dual cell (thick solid line) associated with a mesh node (right).

A simple forward Euler discretisation of the time derivative leads to an iterative update of the nodal solution values which is generally written as

$$u_i^{n+1} = u_i^n + \frac{\Delta t}{S_i} \sum_{j \in \cup \Delta_i} \alpha_i^j \phi_j, \quad (5)$$

where Δt is the time-step, S_i is the area of the median dual cell surrounding node i (one third of the total area of the triangles with a vertex at i , see the right hand side of Figure 1), α_i^j is the distribution coefficient which indicates the appropriate proportion of the fluctuation ϕ_j to be sent from cell j to node i , and $\cup \Delta_i$ represents the set of cells with vertices at node i . The time derivative term in this construction is included here purely as a device for iterating to the steady state.

The most useful fluctuation distribution schemes have been designed so that they satisfy a range of useful properties [30].

Positivity ensures that the numerical approximations are free of unphysical oscillations, which can appear in the vicinity of sharp changes in the solution. This is simple to ensure when the underlying representation of the dependent variable is piecewise linear, but becomes far more challenging when higher degree polynomials are considered [16].

Linearity preservation ensures that the distribution of a fluctuation evaluated exactly with respect to a $(k - 1)^{\text{th}}$ degree polynomial representation

of the flux will lead to a k^{th} order accurate scheme [5]. It is assured as long as the distribution coefficients α_i^j are bounded.

Conservation ensures that discontinuities are captured correctly, and is assured as long as

$$\sum_{i \in \Delta_j} \alpha_i^j = 1 \quad \forall j, \quad (6)$$

where Δ_j represents the set of nodes at the vertices of cell j , *i.e.* the whole of each fluctuation must be sent to the nodes.

Compactness aids the efficiency of the algorithm, especially when parallelisation is considered. For a piecewise linear representation this simply restricts the schemes so that a cell's fluctuation is only distributed to its own vertices.

Continuous dependence of the distribution coefficients α on both the dependent variable u and the advection velocity $\vec{\lambda}$ helps to avoid limit cycles and facilitates smooth convergence to the steady state.

Upwinding is typically introduced for physical realism but its underlying principle is that the discrete form should propagate signals in the same direction and with the same speed as those which appear in the mathematical/physical model, and this seems to facilitate the construction of positive schemes, provides rapid and smooth convergence to the steady state and simplifies the imposition of boundary conditions.

Note that, in line with Godunov's theorem, linear schemes of this form cannot be both positive and linearity preserving [13].

This framework has led to a range of upwind schemes based on a continuous piecewise linear representation of the dependent variable. The three most commonly used, which will be applied in this work, are as follows.

The N scheme is a linear scheme with all the desired properties except linearity preservation. There are many equivalent ways to write down the distribution coefficients for this scheme but, for the purposes of the description here, they will be defined by

$$(\alpha_i^j)^N \phi_j = (\phi_i^j)^N = k_i^+ \left(\sum_{l \in \Delta_j} k_l^- \right)^{-1} \sum_{l \in \Delta_j} k_l^- (u_i - u_l), \quad (7)$$

where $k_i^\pm = \frac{1}{2}(k_i \pm |k_i|)$ with the k_i defined by (4). The distribution coefficients $(\alpha_i^j)^N$ can be derived easily from this. The N scheme is guaranteed to be positive for a time-step of

$$\Delta t \leq \frac{S_i}{\sum_{j \in \cup \Delta_i} (k_i^j)^+} \quad \forall \text{ nodes } i. \quad (8)$$

The LDA scheme is a linear scheme with all the desired properties except

positivity. The distribution coefficients can be written as

$$(\alpha_i^j)^{LDA} = k_i^+ \left(\sum_{l \in \Delta_j} k_l^+ \right)^{-1}. \quad (9)$$

The PSI scheme is a nonlinear scheme with all the desired properties. Its distribution coefficients are most easily defined in terms of those of the linear schemes, either by limiting the distribution coefficients of the N scheme, using

$$(\alpha_i^j)^{PSI} = \frac{[(\alpha_i^j)^N]^+}{\sum_{l \in \Delta_j} [(\alpha_l^j)^N]^+}, \quad (10)$$

or by writing it as a weighted combination of the N and LDA scheme coefficients. It is clear from (10) that $(\alpha_i^j)^{PSI} \in [0, 1]$ and simple to show that the scheme is positive, with a less strict time-step constraint than that of the N scheme. Its disadvantages when compared to the linear schemes are the difficulty with which it can be generalised to nonlinear systems of equations and the slower convergence to the steady state it exhibits, even for linear, scalar systems [1].

Details of all of these schemes can be found in [2,13,30].

3 Nonlinear Systems of Equations

Consider the system of conservation laws given by

$$\underline{U}_t + \vec{\nabla} \cdot \vec{\underline{F}} = \underline{0} \quad \text{or} \quad \underline{U}_t + \vec{\mathbf{A}} \cdot \vec{\nabla} \underline{U} = \underline{0} \quad (11)$$

with appropriate initial and boundary conditions on a domain Ω . \underline{U} is now the vector of conserved variables, $\vec{\underline{F}}$ represents the conservative fluxes and $\vec{\mathbf{A}}$ contains the flux Jacobian matrices. The fluctuation associated with this system is given (*cf.* Equation (2)) by

$$\underline{\Phi} = - \int_{\Delta} \vec{\mathbf{A}} \cdot \vec{\nabla} \underline{U} \, d\Omega = - \int_{\Delta} \vec{\nabla} \cdot \vec{\underline{F}} \, d\Omega = \oint_{\partial\Delta} \vec{\underline{F}} \cdot \vec{n} \, d\Gamma, \quad (12)$$

in which \vec{n} is again the inward pointing unit normal.

It is important to be able to correctly approximate the position and strength of nonlinear discontinuities, such as shocks, which can occur in solutions of nonlinear systems. Hence the scheme should be conservative, *i.e.* in the absence of internal sources and sinks, the total change in the conserved variables should depend only on the flux through the boundary of the domain. A fluctuation distribution scheme for the homogeneous equations (11) is conservative if the

fluctuation on which it is based (which must be fully distributed to the mesh nodes) satisfies

$$\underline{\Phi} = \oint_{\partial\Delta} \widehat{\underline{F}} \cdot \vec{n} \, d\Gamma \quad (13)$$

for some continuous approximation $\widehat{\underline{F}}$ of the flux.

For the system used in this work a conservative linearisation exists under the assumption that a particular set of variables (known as the parameter vector variables, originally defined by Roe for his approximate Riemann solver [22]) vary linearly within each mesh cell, and the discrete fluctuation can be written (*cf.* Equation (3))

$$\underline{\Phi} = -S_{\Delta} \widetilde{\underline{A}} \cdot \widetilde{\nabla} \underline{U} = -\frac{1}{2} \sum_{i \in \Delta} \underline{U}_i \widetilde{\underline{A}} \cdot \vec{n}_i = -\sum_{i \in \Delta} \mathbf{K}_i \underline{U}_i, \quad (14)$$

where

$$\mathbf{K}_i = \frac{1}{2} \widetilde{\underline{A}} \cdot \vec{n}_i, \quad (15)$$

in line with Equation (4), and the symbol \sim indicates an appropriately linearised quantity.

The existence of a conservative linearisation is advantageous because it leads to a simple approximation of the flux Jacobians which provides a natural definition of the \mathbf{K}_i parameters which are subsequently used to distribute the fluctuation. Typically, a linearisation of this type leads to approximate Jacobians and gradients of the form

$$\widetilde{\underline{A}} = \frac{\partial \widetilde{\underline{F}}}{\partial \underline{U}}(\underline{Z}) \quad \text{and} \quad \widetilde{\nabla} \underline{U} = \frac{\partial \underline{U}}{\partial \underline{Z}}(\underline{Z}) \vec{\nabla} \underline{Z} \quad (16)$$

for some piecewise linear set of parameter vector variables \underline{Z} (and hence piecewise constant $\vec{\nabla} \underline{Z}$). This greatly facilitates the application of the fluctuation distribution approach to this system of equations, although it would still be possible (subject to the loss of strict satisfaction of properties such as positivity) even if there was no conservative linearisation available [3,10].

In the case considered here \underline{Z} in a mesh cell is simply the arithmetic mean of the values of \underline{Z} at the cell vertices. The construction of the conservative linearisation is also very simple in the scalar cases of divergence-free linear advection and the inviscid Burgers' equation (both used later in this paper), since $z = u$ provides an appropriate set of variables for the averaging.

3.1 Wave Decomposition Models

One approach to carrying out the distribution of the fluctuation given in (14) is to attempt to decompose it into simpler components which can each be distributed according to the schemes described in the Section 2. This can be done by attempting to diagonalise the system using a similarity transformation, *i.e.* writing

$$\underline{\Phi} = -S_{\Delta} \widetilde{\mathbf{R}} \widetilde{\mathbf{A}}' \widetilde{\mathbf{R}}^{-1} \cdot \widetilde{\nabla} \underline{U}, \quad (17)$$

where $\widetilde{\mathbf{R}}$ is chosen so that the component matrices of $\widetilde{\mathbf{A}}'$ are diagonal. Unfortunately the component matrices of $\widetilde{\mathbf{A}}$ are not, in general, simultaneously diagonalisable so the resulting decomposition given by Equation (17) actually takes the form

$$\underline{\Phi} = \sum_{l=1}^{N_w} \phi^l \widetilde{\mathbf{r}}^l \quad \text{where} \quad \phi_l = -S_{\Delta} \widetilde{\lambda}^l \cdot \widetilde{\nabla} W^l + \widetilde{q}^l, \quad (18)$$

in which N_w is the number of components (or waves) in the decomposition (4 for the two-dimensional Euler equations), $\widetilde{\mathbf{r}}^l$ are the columns of the matrix $\widetilde{\mathbf{R}}$, W^l are the transformed (characteristic) variables, defined purely in terms of their gradients, *i.e.*

$$\widetilde{\nabla} W^l = \widetilde{\mathbf{R}}^{-1} \widetilde{\nabla} \underline{U}, \quad (19)$$

$\widetilde{\lambda}^l$ are the wave speeds, given by the diagonal elements of $\widetilde{\mathbf{A}}'$, and \widetilde{q}^l are derived from the remaining off-diagonal terms of $\widetilde{\mathbf{A}}'$. The ϕ^l all contain an advective term which can be distributed using any of the scalar schemes of Section 2 and the additional \widetilde{q}^l terms are dealt with by distributing the whole of each ϕ^l using the coefficients derived for the homogeneous equation [19]. The $\widetilde{\mathbf{r}}^l$ provide the projection of the resulting signals, sent by the scalar component to the cell vertices, back on to the conservative variables before they are used in the final update

$$\underline{U}_i^{n+1} = \underline{U}_i^n + \frac{\Delta t}{S_i} \sum_{j \in \mathcal{U}\Delta_i} \sum_{l=1}^{N_w} (\alpha_i^j)^l \phi_j^l \widetilde{\mathbf{r}}_j^l. \quad (20)$$

The most successful schemes developed incorporate a preconditioning matrix within $\widetilde{\mathbf{R}}$ which allows the system to be decoupled in an optimal fashion [19]. In supercritical flow, where the steady state Euler equations are completely hyperbolic, this leads to complete decoupling, but for subcritical flow only two components can be decoupled, leaving (in two dimensions) a 2×2 elliptic subsystem.

The results shown in this paper use the Elliptic-Hyperbolic decomposition of Roe and Mesaros [17,26], which applies the PSI scheme to the decoupled com-

ponents and a Lax-Wendroff-style distribution of the form (in two dimensions)

$$(\alpha_i^j)^{LW} = \frac{1}{3}\mathbf{I} + \frac{\Delta t}{4S_{\Delta_j}} \widetilde{\mathbf{A}} \cdot \vec{n}_i^j \quad (21)$$

to the elliptic subsystem in subcritical regions, *i.e.* a pair of waves from (20) are treated as a coupled subsystem instead of considering the nonzero \tilde{q}^l in (18) as source terms. The scheme is regularised through the critical point in the manner described in [17], in which the preconditioning matrix depends on a function ϵ of the local Mach number M . It is stated in [17] that it should satisfy $\epsilon(0) = \frac{1}{2}$ and $\epsilon(1) = 1$: in this work it is defined so that it approaches these values smoothly, *i.e.* $\epsilon'(0) = \epsilon'(1) = 0$, leading to

$$\epsilon(M) = \begin{cases} -M^3 + \frac{3}{2}M^2 + \frac{1}{2} & \text{for } 0 \leq M \leq 1 \\ 1 & \text{for } M > 1. \end{cases} \quad (22)$$

3.2 Matrix Distribution Schemes

A more robust alternative to wave decomposition was developed to incorporate multidimensional upwinding within matrix distribution coefficients [12,19,30]. Using Equation (14), the two-dimensional fluctuation can be written as

$$\underline{\Phi} = - \sum_{i \in \Delta} \mathbf{K}_i \underline{U}_i \quad \text{where} \quad \mathbf{K}_i = \frac{1}{2} \widetilde{\mathbf{A}} \cdot \vec{n}_i. \quad (23)$$

Now, unlike $\widetilde{\mathbf{A}}$ which had components which weren't necessarily simultaneously diagonalisable, the \mathbf{K}_i can easily be diagonalised for the Euler equations, so

$$\mathbf{K}_i = \widetilde{\mathbf{R}}_i \widetilde{\mathbf{\Lambda}}_i \widetilde{\mathbf{R}}_i^{-1} \quad \text{giving} \quad \mathbf{K}_i^\pm = \widetilde{\mathbf{R}}_i \widetilde{\mathbf{\Lambda}}_i^\pm \widetilde{\mathbf{R}}_i^{-1}. \quad (24)$$

in which $\widetilde{\mathbf{R}}_i$ is the matrix of right eigenvectors of \mathbf{K}_i and $\widetilde{\mathbf{\Lambda}}_i^\pm = \frac{1}{2}(\widetilde{\mathbf{\Lambda}}_i \pm |\widetilde{\mathbf{\Lambda}}_i|)$, $|\widetilde{\mathbf{\Lambda}}_i|$ being the diagonal matrix of the absolute values of the eigenvalues of \mathbf{K}_i . In fact the \mathbf{K} matrices take the form of the linearised flux Jacobians which occur in the standard multidimensional extension of Roe's flux difference splitting [22].

The two linear scalar schemes described in Section 2 have simple matrix forms. The system N scheme is defined (*cf.* Equation (7)) by

$$(\underline{\Phi}_i^j)^N = \mathbf{K}_i^+ \left(\sum_{l \in \Delta_j} \mathbf{K}_l^- \right)^{-1} \sum_{l \in \Delta_j} \mathbf{K}_l^- (\underline{U}_i - \underline{U}_l), \quad (25)$$

while the system LDA scheme is given (*cf.* Equation (9)) by

$$(\underline{\Phi}_i^j)^{LDA} = \mathbf{K}_i^+ \left(\sum_{l \in \Delta_j} \mathbf{K}_l^+ \right)^{-1} \underline{\Phi}. \quad (26)$$

The nonlinear PSI scheme is more difficult to generalise to nonlinear systems of equations, since the N scheme does not have explicit matrix coefficients. It is therefore not possible to carry out a “limiting” procedure of the form defined by (10). Instead, a blended scheme is typically used, *i.e.*

$$(\underline{\Phi}_i)^B = \mu \underline{\Phi}_i^N + (1 - \mu) \underline{\Phi}_i^{LDA}, \quad (27)$$

where μ is chosen so that (i) the LDA scheme dominates in smooth regions, (ii) the N scheme is applied near to discontinuities, and (iii) the overall scheme is positive (or nearly so). In this work the very simple form given by

$$\mu = \frac{|\underline{\Phi}|}{|\underline{\Phi}_1^N| + |\underline{\Phi}_2^N| + |\underline{\Phi}_3^N|} \quad (28)$$

is chosen, following the work of [15], though more sophisticated options are available [2].

The overall update of the matrix distribution schemes takes the form

$$\underline{U}_i^{n+1} = \underline{U}_i^n + \frac{\Delta t}{S_i} \sum_{j \in \mathcal{U}\Delta_i} \underline{\Phi}_i^j. \quad (29)$$

4 A Discontinuous Scheme

4.1 Scalar Conservation Laws

A continuous representation of u was assumed throughout the discussion in Section 2. In that case, the integral of the scalar conservation law (1) over Ω was divided between the mesh cells, leading to the fluctuations (2)/(3) which were used to update u , via (5), in a conservative manner.

If the discrete representation of u is allowed to be discontinuous across the mesh edges then the integral of the flux divergence over the whole domain includes terms arising from these discontinuities, *i.e.*

$$\int_{\Omega} \vec{\nabla} \cdot \vec{f} \, d\Omega = \sum_{j=1}^{N_c} \int_{\Delta_j} \vec{\nabla} \cdot \vec{f} \, d\Omega + \sum_{j=1}^{N_e} \int_{|j} \vec{\nabla} \cdot \vec{f} \, d\Omega, \quad (30)$$

in which $|$ is used to represent a mesh edge (face in three dimensions) and N_c , N_e are the numbers of cells and edges, respectively. Each edge can be thought of as the limit of a rectangle as its width tends to zero, as illustrated on the left hand side of Figure 2, which leads to an expression for the fluctuation associated with a mesh edge:

$$\psi = -\lim_{\epsilon \rightarrow 0} \int_{\square_\epsilon} \vec{\nabla} \cdot \vec{f} d\Omega = \lim_{\epsilon \rightarrow 0} \oint_{\partial \square_\epsilon} \vec{f} \cdot \vec{n} d\Gamma = \int_{|} [\vec{f} \cdot \vec{n}] d\Gamma, \quad (31)$$

in which $[]$ represents the jump in a quantity across the edge, the sign of the difference being dictated by the direction chosen for \vec{n} . This is simply the integral along the cell edge (in three dimensions this would be the integral over the cell face) of the flux difference across it.

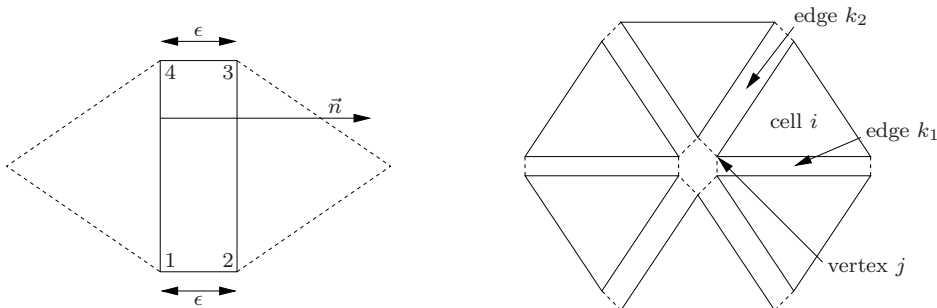


Fig. 2. The mesh structure for the discontinuous fluctuation distribution at an edge (left) and around a node (right).

Under the assumption that a conservative linearisation exists for the flux difference [22], the edge-based fluctuation given in (31) can be evaluated exactly, giving

$$\psi = -\sum_{l=1}^{N_q} w_l \tilde{\lambda}_l \cdot \vec{n} [u_l], \quad (32)$$

in which N_q is the number of quadrature points used in integrating (31), w_l are the quadrature weights and $\tilde{\lambda}_l = \partial \vec{f}(\tilde{u}_l) / \partial u$ (\tilde{u}_l being a conservative average of the two values for u at the specified quadrature point). The direction of \vec{n} indicated in Figure 2 is consistent with the jump in the solution being given by $[u] = u_{right} - u_{left}$. For all of the equations considered in this work, and given that it has been assumed here that the parameter vector variables vary linearly within each mesh cell (and hence along each mesh edge), Simpson's rule is accurate enough to integrate (31) exactly. Although it is not essential to make use of this linearisation, doing so fits naturally with the existing framework, especially the extension to systems of equations, and makes it simpler to demonstrate the satisfaction of properties such as positivity.

In order to ensure that these edge fluctuations can be used as part of a positive scheme, (32) is rewritten (using the numbering indicated on the left of Figure

2) as

$$\psi = \frac{1}{2} \widehat{\lambda}_{12} \cdot \vec{n} (u_1 - u_2) + \frac{1}{2} \widehat{\lambda}_{43} \cdot \vec{n} (u_4 - u_3). \quad (33)$$

The $\widehat{\lambda}$ are conservatively averaged values, but they are not defined as they would be within each mesh cell and therefore differ from $\widetilde{\lambda}$. Instead they are defined here to be

$$\widehat{\lambda}_{12} = \frac{1}{3} \left(\vec{\lambda}_1 + \vec{\lambda}_2 + \frac{\vec{\lambda}_3 + \vec{\lambda}_4}{2} \right), \quad \widehat{\lambda}_{43} = \frac{1}{3} \left(\vec{\lambda}_3 + \vec{\lambda}_4 + \frac{\vec{\lambda}_1 + \vec{\lambda}_2}{2} \right). \quad (34)$$

Note that the decomposition given in (34) is not unique. In fact the existence of a conservative linearisation within any triangular cell means that an equivalent expression can be derived by considering ψ to be the sum of fluctuations over two degenerate triangular cells. In the notation of Figure 2 these triangles could be chosen to be either \triangle_{123} and \triangle_{134} , which give

$$\widehat{\lambda}_{12} = \frac{1}{3} (\vec{\lambda}_1 + \vec{\lambda}_2 + \vec{\lambda}_3) \quad \text{and} \quad \widehat{\lambda}_{43} = \frac{1}{3} (\vec{\lambda}_1 + \vec{\lambda}_3 + \vec{\lambda}_4), \quad (35)$$

or \triangle_{124} and \triangle_{234} , which give

$$\widehat{\lambda}_{12} = \frac{1}{3} (\vec{\lambda}_1 + \vec{\lambda}_2 + \vec{\lambda}_4) \quad \text{and} \quad \widehat{\lambda}_{43} = \frac{1}{3} (\vec{\lambda}_2 + \vec{\lambda}_3 + \vec{\lambda}_4). \quad (36)$$

In this work, the symmetric definition given by (34) is used, which is simply the average of the two situations given above. Each formulation leads to the same value for the edge fluctuation ψ in (33), they only differ in the precise form of the resulting distribution coefficients.

The fluctuation ψ in (33) can now be distributed to the four cell vertices (two pairs of coincident vertices) associated with the edge, and the form shown in (33) indicates clearly how it can be distributed in a positive manner according to the direction of the local linearised advection velocity, *i.e.* for a single edge, ignoring any contributions from other cells or edges,

$$\begin{aligned} \frac{S_1}{3} u_1 &\rightarrow \frac{S_1}{3} u_1 + \frac{\Delta t}{2} [\widehat{\lambda}_{12} \cdot \vec{n}]^- (u_1 - u_2) = \frac{S_1}{3} u_1 + \Delta t \alpha_1 \psi \\ \frac{S_2}{3} u_2 &\rightarrow \frac{S_2}{3} u_2 + \frac{\Delta t}{2} [\widehat{\lambda}_{12} \cdot \vec{n}]^+ (u_1 - u_2) = \frac{S_2}{3} u_2 + \Delta t \alpha_2 \psi \\ \frac{S_3}{3} u_3 &\rightarrow \frac{S_3}{3} u_3 + \frac{\Delta t}{2} [\widehat{\lambda}_{43} \cdot \vec{n}]^+ (u_4 - u_3) = \frac{S_3}{3} u_3 + \Delta t \alpha_3 \psi \\ \frac{S_4}{3} u_4 &\rightarrow \frac{S_4}{3} u_4 + \frac{\Delta t}{2} [\widehat{\lambda}_{43} \cdot \vec{n}]^- (u_4 - u_3) = \frac{S_4}{3} u_4 + \Delta t \alpha_4 \psi, \end{aligned} \quad (37)$$

where $[]^\pm$ signifies the positive/negative part of the quantity and S_l ($l = 1, 2, 3, 4$) is the area of the mesh cell whose vertex is being updated. It is easy

to see that $\alpha_1 + \alpha_2 + \alpha_3 + \alpha_4 = 1$, so the distribution is conservative. It is also continuous, compact and upwind, closely resembling the standard first order upwind scheme, except that the pairs of nodes (1, 2) and (3, 4) are coincident. However, it should be noted that one important property is lost completely: while the schemes mentioned in Section 2 all drop to first order accuracy for time-dependent problems, this scheme is not time-accurate at all.

Each mesh node now corresponds to many cell vertices and multiple values of u . When the new edge-based fluctuations are distributed along with the original cell-based fluctuations each u_i^j (the value associated with vertex i of cell j) can receive contributions from precisely one cell and two edges (subject to the application of boundary conditions), leading to the update

$$(u_i^j)^{n+1} = (u_i^j)^n + \frac{3\Delta t}{S_j} \left(\alpha_i^j \phi_j + \alpha_i^{k_1} \psi_{k_1} + \alpha_i^{k_2} \psi_{k_2} \right), \quad (38)$$

in which the indices follow the annotation shown on the right hand side of Figure 2 and S_j is the area of cell j . The distribution coefficients for the edge fluctuations can be found easily from (33) and (37). Note that it is easy to show that the contribution due to the degenerate polygon which appears at each mesh node (see the centre of the right hand diagram in Figure 2) is zero.

It should be noted that applying (37), or an appropriate higher order version, to any continuous polynomial steady state leads to zero contributions from the edges, since $u_1 = u_2$ and $u_3 = u_4$. Therefore, any continuous steady state will always be preserved by this distribution of the edge-based fluctuations, so the overall order of accuracy is governed by the cell-based fluctuation distribution scheme chosen. This leads to the following:

Proposition (Linearity Preservation). *The discontinuous fluctuation distribution scheme defined by (38) is linearity preserving as long as the continuous fluctuation distribution scheme defined by (5) with the same cell-based distribution coefficients α_i^j has this property.*

It is possible to modify the edge distribution given by (37) by applying precisely the technique presented in (10) which creates bounded distribution coefficients from ones which give a positive scheme (and was used to impose linearity preservation on the distribution of the cell-based fluctuation), *i.e.*

$$\alpha_i \rightarrow \frac{(\alpha_i)^+}{\sum_{l \in \Delta_j} (\alpha_l)^+}. \quad (39)$$

However, the above proposition suggests that this is not necessary and, in practice, applying (39) has little effect on the numerical results.

The overall discontinuous fluctuation distribution scheme, as defined by the iteration in (38) is conservative, positive for an appropriate limit on Δt , given

by

$$\Delta t \leq \frac{S_j/3}{\sum_{l \in \Delta_j} (k_l^j)^+} \quad \forall \text{ cells } j, \quad (40)$$

linearity preserving, compact, upwind and continuous (when the underlying cell- and edge-based distributions are).

The use of flux differences rather than fluxes when dealing with a discontinuity in the discrete representation of the solution is useful because it doesn't require the definition of any form of averaged "numerical" flux at the discontinuity. It also accounts for the full variation of the solution along the edge, instead of assuming that all of the activity occurs at its midpoint, and allows for a natural treatment of source/balance terms. On the other hand, when fluxes are used, the existence of a conservative linearisation which facilitates conservation is significantly less important, which simplifies the implementation of h - and p -adaptivity.

4.2 Nonlinear Systems of Equations

The extension to nonlinear systems of equations of the form given in (11) is straightforward, assuming that a conservative linearisation exists [11,22] and that the resulting set of parameter vector variables vary linearly within each mesh cell. The cell fluctuations can still be treated in the manner described in Section 3, but the edge fluctuations (31) are now given by

$$\underline{\Psi} = \int_{\Gamma} [\underline{\vec{F}} \cdot \vec{n}] d\Gamma. \quad (41)$$

Given that the linearisation is constructed under the assumption of the linear variation of a set of parameter vector variables, and that $\underline{\vec{F}}$ is quadratic in these variables, it is again enough to use Simpson's rule to carry out the integration exactly. Using the numbering system illustrated in Figure 2, the edge fluctuation (33) can be written (*cf.* Equation (16))

$$\underline{\Psi} = \frac{1}{2} \widehat{\mathbf{A}}_{12} \cdot \vec{n} (\underline{U}_1 - \underline{U}_2) + \frac{1}{2} \widehat{\mathbf{A}}_{43} \cdot \vec{n} (\underline{U}_4 - \underline{U}_3), \quad (42)$$

in which $\widehat{\mathbf{A}} = \vec{\mathbf{A}}(\widehat{\underline{Z}})$ and the differences across the edge, $\widehat{\Delta \underline{U}} := \frac{\partial \underline{U}}{\partial \underline{Z}}(\widehat{\underline{Z}}) \Delta \underline{Z}$ (*cf.* Equation (16)), are defined using averages of the parameter vector variables [22] analogous to those shown for scalar advection in (34), *i.e.*

$$\begin{aligned} \widehat{\underline{Z}}_{12} &= \frac{1}{3} \left(\underline{Z}_1 + \underline{Z}_2 + \frac{\underline{Z}_3 + \underline{Z}_4}{2} \right) \\ \widehat{\underline{Z}}_{43} &= \frac{1}{3} \left(\underline{Z}_3 + \underline{Z}_4 + \frac{\underline{Z}_1 + \underline{Z}_2}{2} \right). \end{aligned} \quad (43)$$

The $\underline{\Psi}$ could easily be distributed directly (using a central scheme, for example) but to retain the positivity of the scalar schemes they are here decomposed using Roe's flux difference splitting [22], via the diagonalisation of the Jacobian matrices in (42) given by

$$\widehat{\mathbf{A}} \cdot \vec{n} = \widehat{\mathbf{R}} \widehat{\mathbf{\Lambda}} \widehat{\mathbf{R}}^{-1}. \quad (44)$$

Upwinding (and hence positivity) is imposed using the wave velocities which appear in the diagonal eigenvalue matrix $\widehat{\mathbf{\Lambda}}$. This allows each of the two components of the edge fluctuation (42) to take the form

$$\sum_{l=1}^{N_w} \psi^l \tilde{\underline{x}}^l \quad \text{where} \quad \psi_l = \widehat{\lambda}^l \cdot \Delta \widehat{W}^l, \quad (45)$$

in which N_w is the number of components in the decomposition (4 for the two-dimensional Euler equations), $\tilde{\underline{x}}^l$ are the eigenvectors of the matrix $\widehat{\mathbf{A}} \cdot \vec{n}$ and the columns of the matrix $\widehat{\mathbf{R}}$, W^l are the characteristic variables ($\Delta \widehat{W}^l = \widehat{\mathbf{R}}^{-1} \Delta \widehat{U}$), and $\widehat{\lambda}^l$ are the wave speeds, given by the eigenvalues of the matrix $\widehat{\mathbf{A}} \cdot \vec{n}$ (the diagonal elements of $\widehat{\mathbf{\Lambda}}$). The fluctuations due to the individual waves are distributed using (37) and their signals projected back to provide updates to the conservative variables using the eigenvectors of $\widehat{\mathbf{A}} \cdot \vec{n}$.

As in the scalar case (38), each cell vertex can receive contributions from one mesh cell and two mesh edges, but these contributions are now decomposed into individual waves or found using matrix distribution schemes.

5 Numerical Experiments

5.1 A Linear Scalar Equation

The first test case considered involves the approximation of steady state solutions of the scalar advection equation,

$$u_t + \vec{\lambda} \cdot \vec{\nabla} u = 0 \quad (46)$$

with velocity $\vec{\lambda} = (y, -x)^T$ over the domain $[-1, 1] \times [0, 1]$, and boundary conditions given by

$$u(x, y) = \begin{cases} 1 & \text{for } -0.65 \leq x \leq -0.35 \text{ and } y = 0 \\ 0 & \text{elsewhere on inflow boundaries.} \end{cases} \quad (47)$$

The square wave profile should be advected in a circular arc without change of shape and the exact solution is given by

$$u(x, y) = \begin{cases} 1 & \text{for } 0.35 \leq r = \sqrt{x^2 + y^2} \leq 0.65 \\ 0 & \text{elsewhere.} \end{cases} \quad (48)$$

In this case $\vec{\nabla} \cdot \vec{\lambda} = 0$, so the advection equation and the conservation law with $\vec{f} = u\vec{\lambda}$ are equivalent and the conservative linearisation is simple [13]. Figure 3 shows that the results obtained using the discontinuous PSI scheme agree closely with those of the standard PSI scheme and confirms that the new scheme is positive: there are no overshoots or undershoots in either set of results.

The above test case uses a discontinuous boundary profile to test for positivity, but a second test case is used here to verify the order of accuracy of the new scheme. It uses the same velocity profile, but a solution profile with continuous fourth derivative, given by the boundary conditions

$$u(x, y) = \begin{cases} G(x) & \text{for } -0.75 \leq x \leq -0.25 \text{ and } y = 0 \\ 0 & \text{elsewhere on inflow boundaries,} \end{cases} \quad (49)$$

in which

$$G(x) = \begin{cases} g(4x + 3) & \text{for } -0.75 \leq x \leq -0.5 \\ g(-4x - 1) & \text{for } -0.5 < x \leq -0.25 \end{cases} \quad (50)$$

where

$$g(x) = x^5(70x^4 - 315x^3 + 540x^2 - 420x + 126). \quad (51)$$

The exact solution to this problem is

$$u(x, y) = \begin{cases} G(r) & \text{for } 0.25 \leq r \leq 0.75 \\ 0 & \text{elsewhere.} \end{cases} \quad (52)$$

It is used to verify the effective order of accuracy of the schemes in the presence of turning points in the solution, using a non-constant (in space) advection velocity, and is applied here on both structured and genuinely unstructured (but uniform) triangular meshes, examples of which are shown in Figure 4.

The results from the continuous and discontinuous PSI schemes illustrated in Figure 5 are very similar, especially on the unstructured meshes when they appear to converge towards each other as the mesh is refined far more rapidly than they converge towards the exact solution. The errors illustrated in the figure and the slopes of the log-log graphs provided in Table 1 suggest that as mesh convergence is approached, the order of accuracy becomes two for both

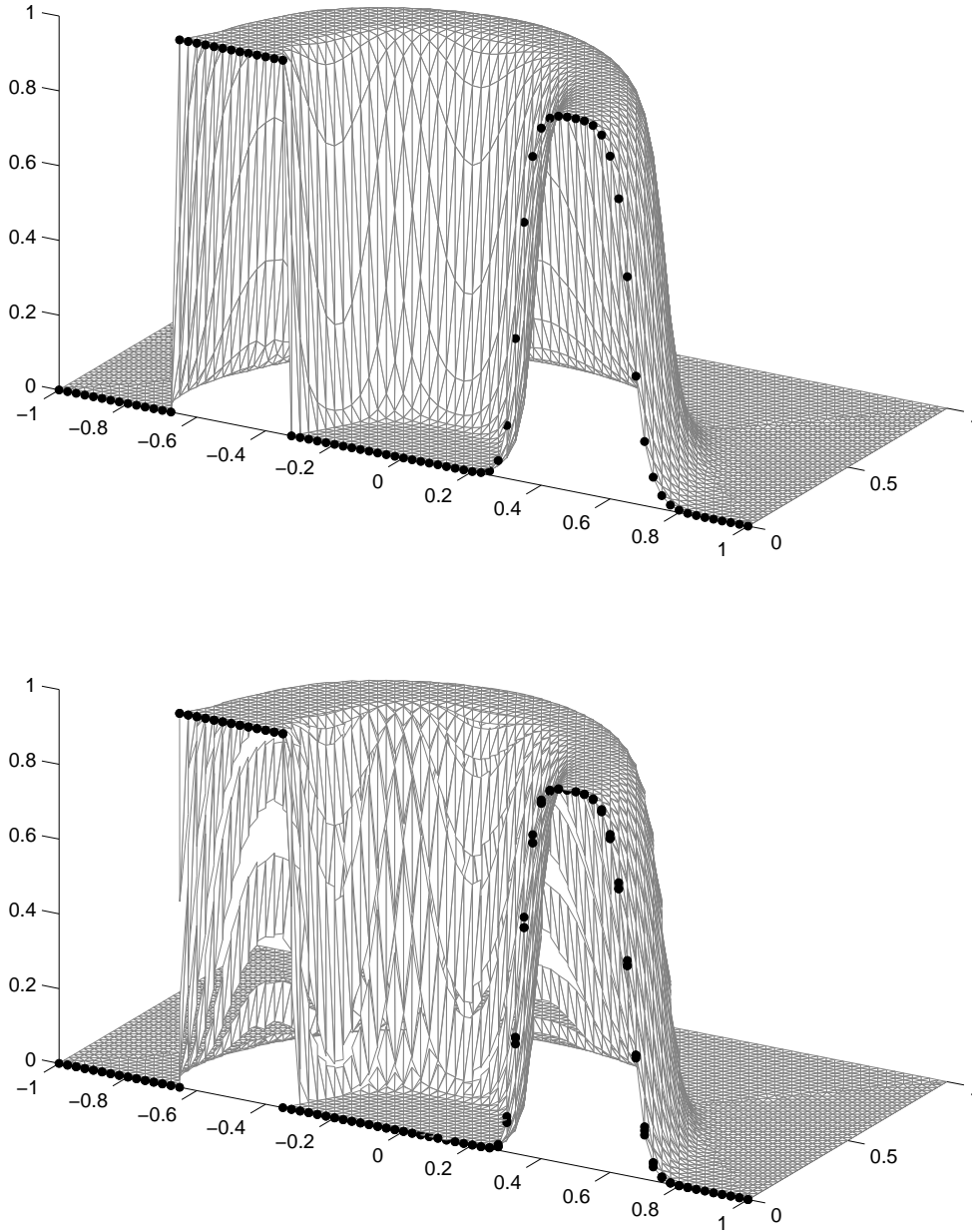


Fig. 3. Circular advection of a square wave profile over an unstructured 3806 node, 7370 cell mesh using continuous (top) and discontinuous (bottom) PSI schemes.

continuous and discontinuous PSI schemes. The edge fluctuations have been distributed using (37) without any modification of the form (39). Applying this to the edge-based fluctuations did not change the order of accuracy shown by the mesh refinement.

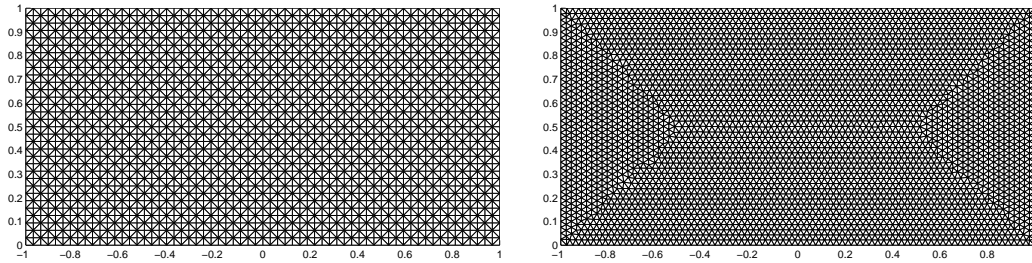


Fig. 4. Representative structured (left) and unstructured (right) meshes used for the scalar advection test cases ($dx \approx \frac{1}{32}$).

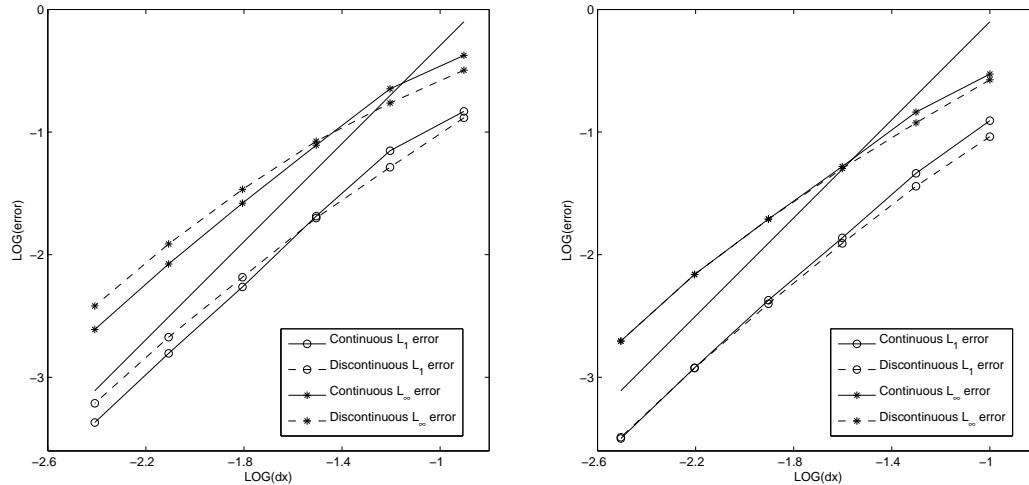


Fig. 5. Errors for the circular advection of a smooth polynomial profile over a series of uniform structured (left) and unstructured (right) meshes. The solid line without symbols is of slope 2 in each graph.

Table 1

Accuracy measures for the uniform structured and unstructured triangular meshes, calculated by comparing the errors obtained on the finest pair of meshes for which results are shown in Figure 5.

Scheme	Structured			Unstructured		
	L_1	L_2	L_∞	L_1	L_2	L_∞
Continuous PSI	1.87	1.85	1.77	1.92	1.90	1.80
Discontinuous PSI	1.79	1.77	1.68	1.87	1.86	1.80

5.2 A Nonlinear Scalar Equation

Discontinuous fluctuation distribution is next applied to a two-dimensional form of the inviscid Burgers' equation which takes the form

$$u_t + \left(\frac{u^2}{2}\right)_x + u_y = 0 \quad \text{or} \quad u_t + \vec{\nabla} \cdot \vec{f} = 0 \quad (53)$$

where $\vec{f} = (\frac{u^2}{2}, u)^T$. It is approximated over the domain $[0, 1] \times [0, 1]$ with boundary conditions on the inflow boundaries ($x = 0$, $x = 1$ and $y = 0$) given by

$$u(x, y) = 1.5 - 2x. \quad (54)$$

This problem has the exact solution

$$u(x, y) = \begin{cases} -0.5 & \text{if } y \geq 0.5 \text{ and } -2(x - 0.75) + (y - 0.5) \leq 0 \\ 1.5 & \text{if } y \geq 0.5 \text{ and } -2(x - 0.75) + (y - 0.5) \geq 0 \\ \max\left(-0.5, \min\left(1.5, \frac{x-0.75}{y-0.5}\right)\right) & \text{otherwise.} \end{cases} \quad (55)$$

Figure 6 compares the numerical solutions obtained using the continuous and discontinuous PSI schemes with the exact solution on a mesh where the edges have been deliberately aligned with the exact shock position. The discontinuous PSI scheme clearly captures the discontinuity in this situation. Close examination of the solution in the vicinity of the shock also reveals that there are no oscillations: the minimum and maximum values of u are exactly -0.5 and 1.5 .

The rates of convergence to the steady state for the scalar test cases are illustrated in Figure 7. In all cases the algorithm converges to machine accuracy, but the discontinuous approach is consistently slower in terms of number of iterations. This is related to the more restrictive constraint on the pseudo-time-step required to impose positivity on the iteration, *cf.* Equations (8) and (40).

5.3 A Nonlinear System of Conservation Laws

Inviscid compressible fluid flow is simulated using the two-dimensional Euler equations which have the form (11) where

$$\underline{U} = \begin{pmatrix} \rho \\ \rho u \\ \rho v \\ e \end{pmatrix} \quad \underline{F} = \begin{pmatrix} \rho u \\ \rho u^2 + p \\ \rho uv \\ u(p + e) \end{pmatrix} \quad \underline{G} = \begin{pmatrix} \rho v \\ \rho uv \\ \rho v^2 + p \\ v(p + e) \end{pmatrix} \quad (56)$$

are, respectively, the vector of conserved variables and the conservative fluxes (components of $\vec{F} = (\underline{F}, \underline{G})$), in which ρ is density, u and v are the x - and y -components of the velocity, p is pressure and e is total energy, related to the

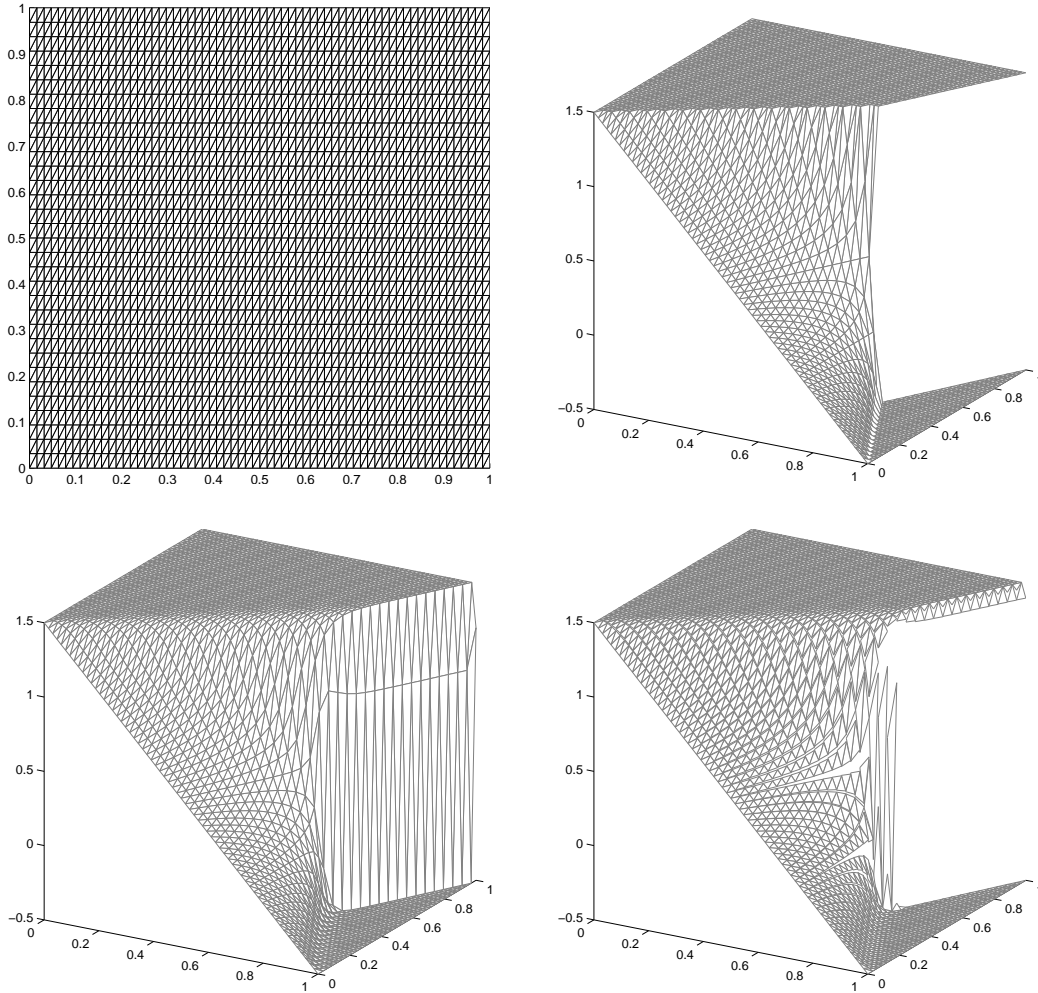


Fig. 6. Inviscid Burgers' equation test case: computational mesh (top left), exact solution on that mesh (top right) and numerical results obtained using continuous (bottom left) and discontinuous (bottom right) PSI schemes.

other variables by an equation of state which, for a perfect gas, is

$$e = \frac{p}{\gamma - 1} + \frac{1}{2}\rho(u^2 + v^2) \quad (57)$$

and where γ is the ratio of specific heat coefficients under constant pressure and constant volume (having the value 1.4 for air).

The test cases used involve flow from left to right through a channel of dimensions $[0, 3] \times [0, 1]$ with additional symmetric bumps situated on the upper and lower walls, which are designed to give a channel breadth of

$$b(x) = \begin{cases} 1 - B \sin^2(\pi(x - 1)) & \text{for } 1 \leq x \leq 2 \\ 1 & \text{otherwise.} \end{cases} \quad (58)$$

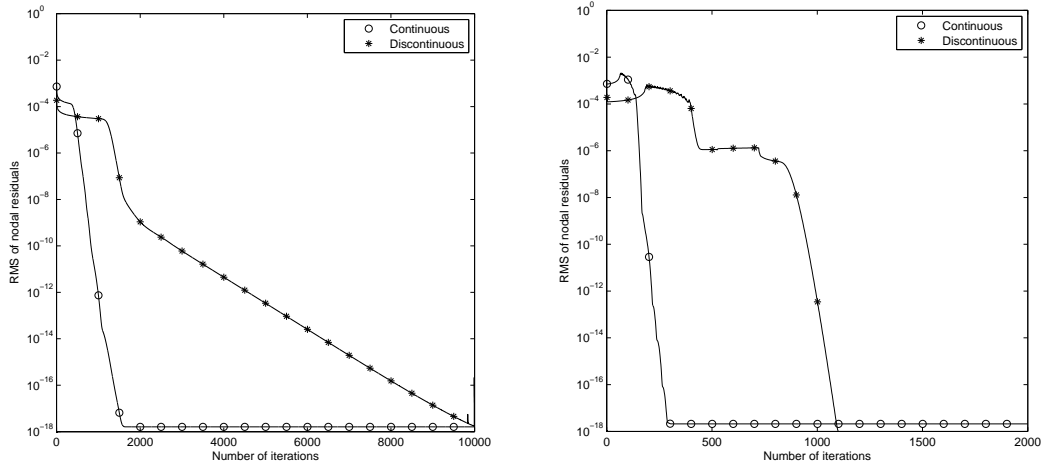


Fig. 7. Convergence histories for the results shown for the scalar advection equation in Figure 3 (left) and for Burgers' equation in Figure 6 (right).

Here $B = 0.1$ has been chosen and three freestream Mach numbers (M_∞) specified at inflow to give subcritical, transcritical and supercritical flows. The unstructured mesh used to produce the results shown is pictured in Figure 8. Figures 9–11 show contour plots of density for each of the three cases and illustrates how the continuous and discontinuous schemes give similar results, though the latter appears to capture discontinuities more sharply. In each case both the Elliptic-Hyperbolic wave decomposition model of Roe and Mesaros [17,26] and the blended matrix distribution scheme defined by (27) and (28) were used to distribute the cell fluctuations, though the blending was switched to the pure LDA scheme ($\mu = 0$ in Equation (27)) for the subcritical case. Roe's flux difference splitting [22] was combined with (37) in the distribution of the edge fluctuations.

The continuous and discontinuous schemes are compared directly in Figure 12, where slices through the solution profiles illustrate their variation along the channel at $x = 0.2$. This shows that the discontinuous scheme captures shocks a little more sharply and, in the transcritical case, this slightly modifies the downstream profile. Results are only shown for the wave decomposition model because those obtained using the matrix distribution scheme exhibited similar features.

Figure 13 shows contours of entropy deviation for the subcritical channel flow. This should be zero throughout the domain for smooth flow and the figure shows that the levels of spurious entropy generated by the indentations in the channel walls are very low for all of the schemes. The plotted contour levels are the same for all of the pictures, indicating that entropy deviation is actually lower for the discontinuous schemes than for the continuous ones in this case.

The convergence histories for the test cases shown in Figures 9-11 are all shown in Figure 14. The figures for the subcritical and transcritical test cases

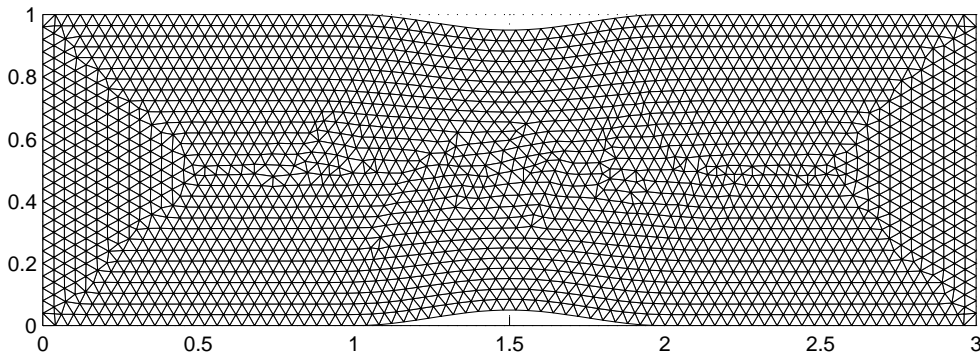


Fig. 8. Unstructured 2242 node, 4282 cell mesh for the 5% constricted channel test cases ($B = 0.1$).

also illustrate the effect of applying the modification suggested by Abgrall [1] (denoted by + in the legend) for improving the convergence properties of the continuous schemes. It should be noted that the explicit scheme used here behaves differently to the implicit scheme presented in [1]. The modification works for the blended scheme applied to the transcritical flow and slightly speeds up the convergence of the blended scheme for the subcritical flow. It actually makes the convergence properties worse in some cases, such as when the wave decomposition scheme is used and when supercritical flow is being modelled with any of the schemes (not shown in the figure). A similar modification was applied to the discontinuous schemes but they showed no improvement. It is clear from Figure 14 that the discontinuous schemes are less robust than their continuous counterparts, an issue that will be addressed in future work.

One final test case is used to illustrate the scheme's ability to capture discontinuities which are aligned with the mesh. It involves the interaction of two horizontal supersonic jets which are suddenly brought into contact [14]. The flow is from left to right through a square domain (here taken to be $[0, 1] \times [-0.5, 0.5]$) where the boundary conditions on the inflow (left) boundary are given by

$$\underline{U} = \begin{cases} (1.4, 3.36, 0.0, 6.532)^T & \text{if } y \geq 0 \\ (0.7, 1.4\sqrt{2}, 0.0, 3.425)^T & \text{otherwise.} \end{cases} \quad (59)$$

The mesh on which this problem has been solved is a 31×91 uniform mesh which has been adjusted so that the edges are closely aligned with the shock and contact discontinuities which appear in the lower half of the domain (see Figure 15). The density and pressure profiles for both the continuous and discontinuous PSI schemes are shown as surface plots in Figure 16 and clearly illustrate the scheme's ability to capture discontinuities. The outflow profiles for density and pressure are compared in Figure 17, showing that the pressure profiles agree closely and the density profiles differ slightly in the left hand

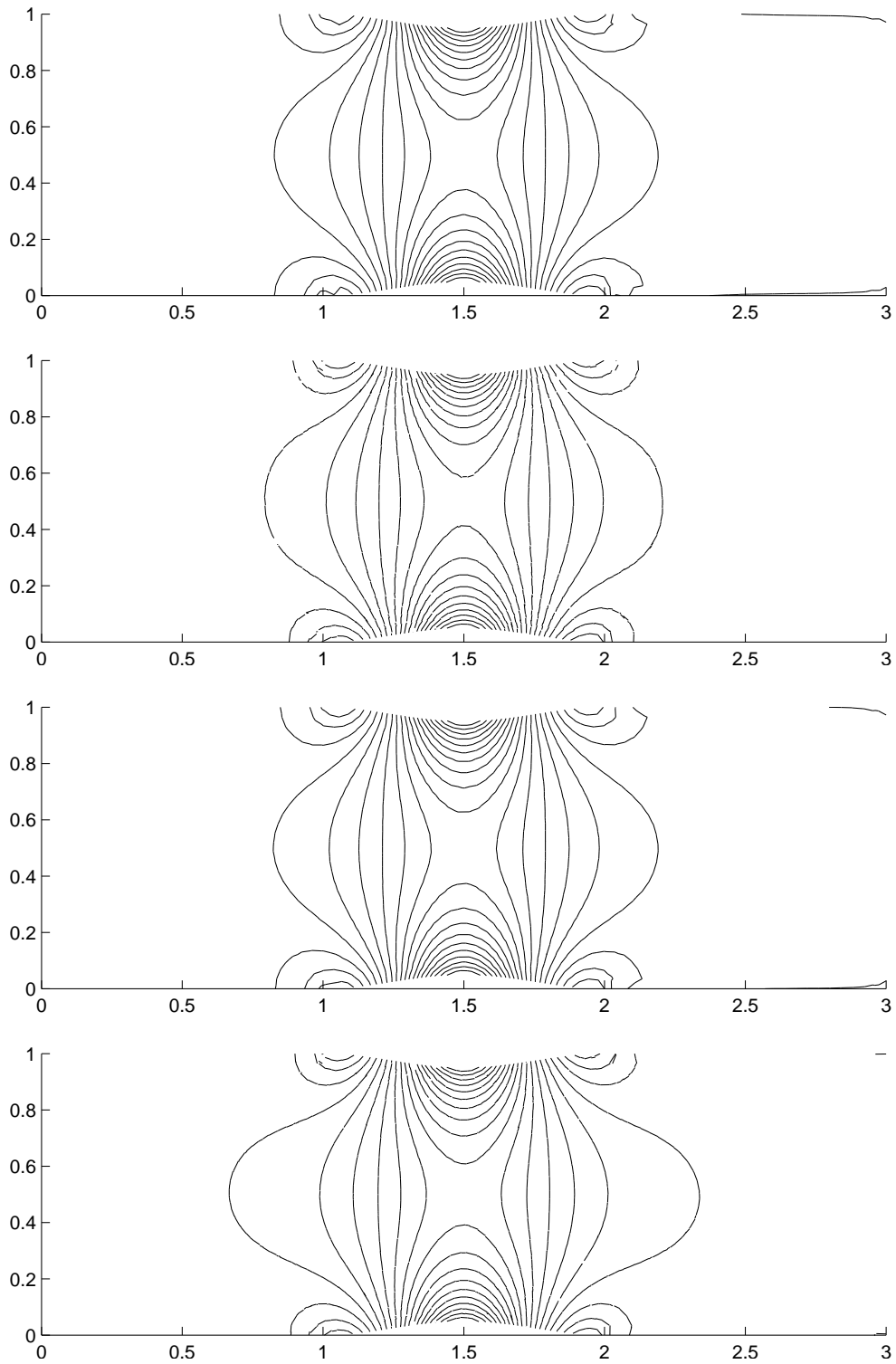


Fig. 9. Contours of density for subcritical flow ($M_\infty = 0.5$) through an indented channel for, from top to bottom, the continuous wave decomposition scheme, the discontinuous wave decomposition scheme, the continuous system LDA scheme and the discontinuous system LDA scheme.

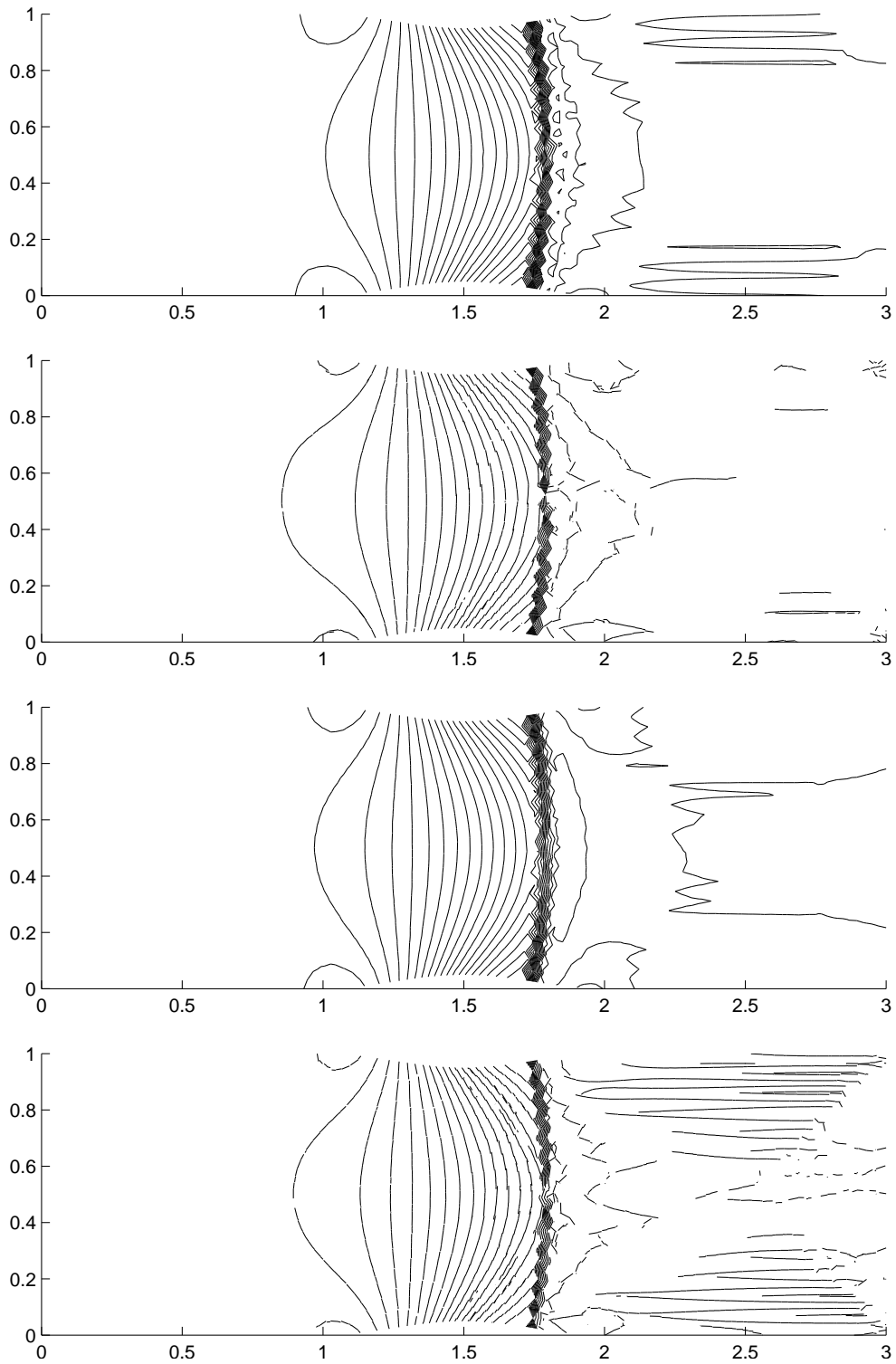


Fig. 10. Contours of density for transcritical flow ($M_\infty = 0.7$) through an indented channel for, from top to bottom, the continuous wave decomposition scheme, the discontinuous wave decomposition scheme, the continuous system blended scheme and the discontinuous system blended scheme.

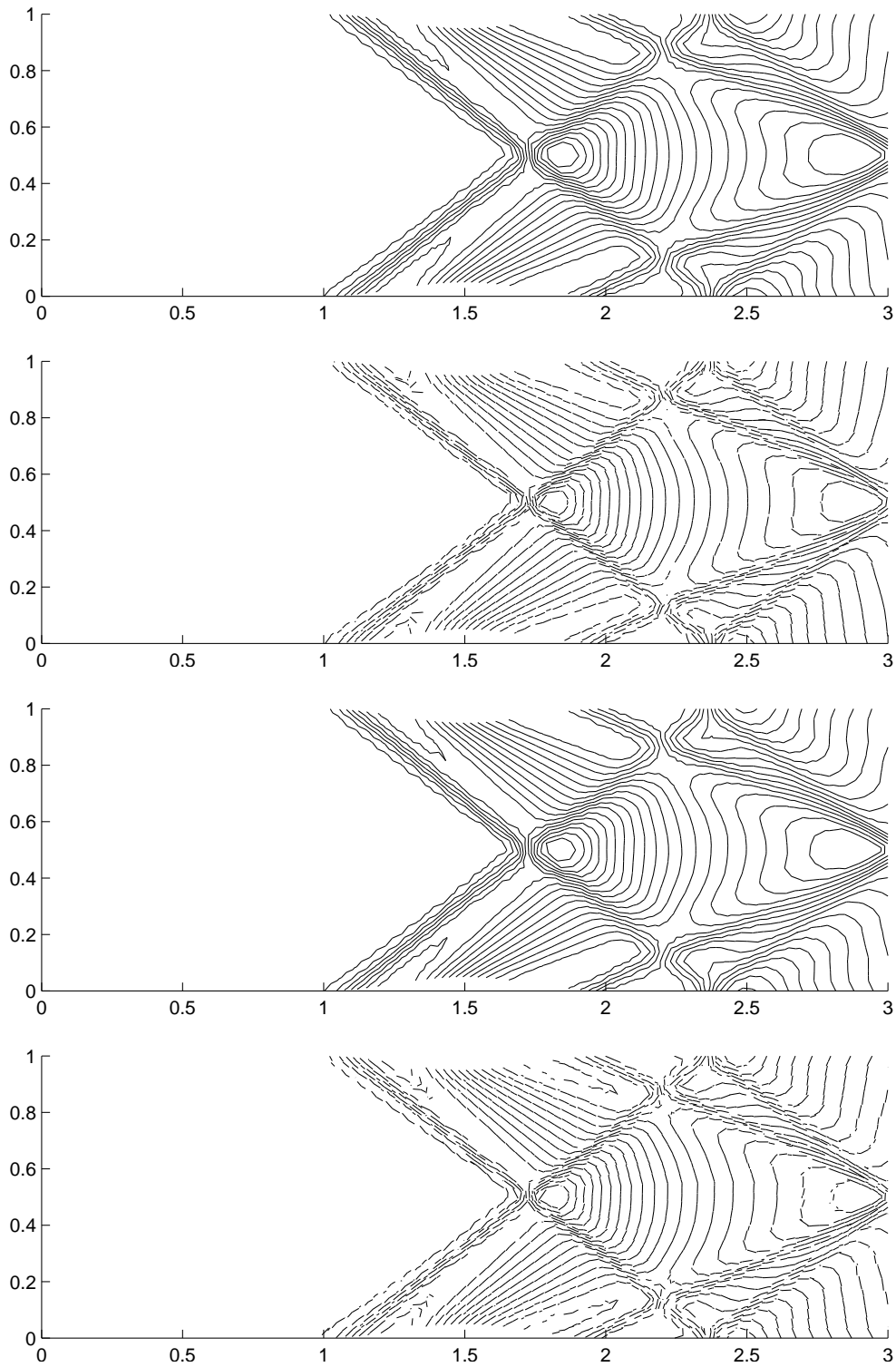


Fig. 11. Contours of density for supercritical flow ($M_\infty = 2.0$) through an indented channel for, from top to bottom, the continuous wave decomposition scheme, the discontinuous wave decomposition scheme, the continuous system blended scheme and the discontinuous system blended scheme.

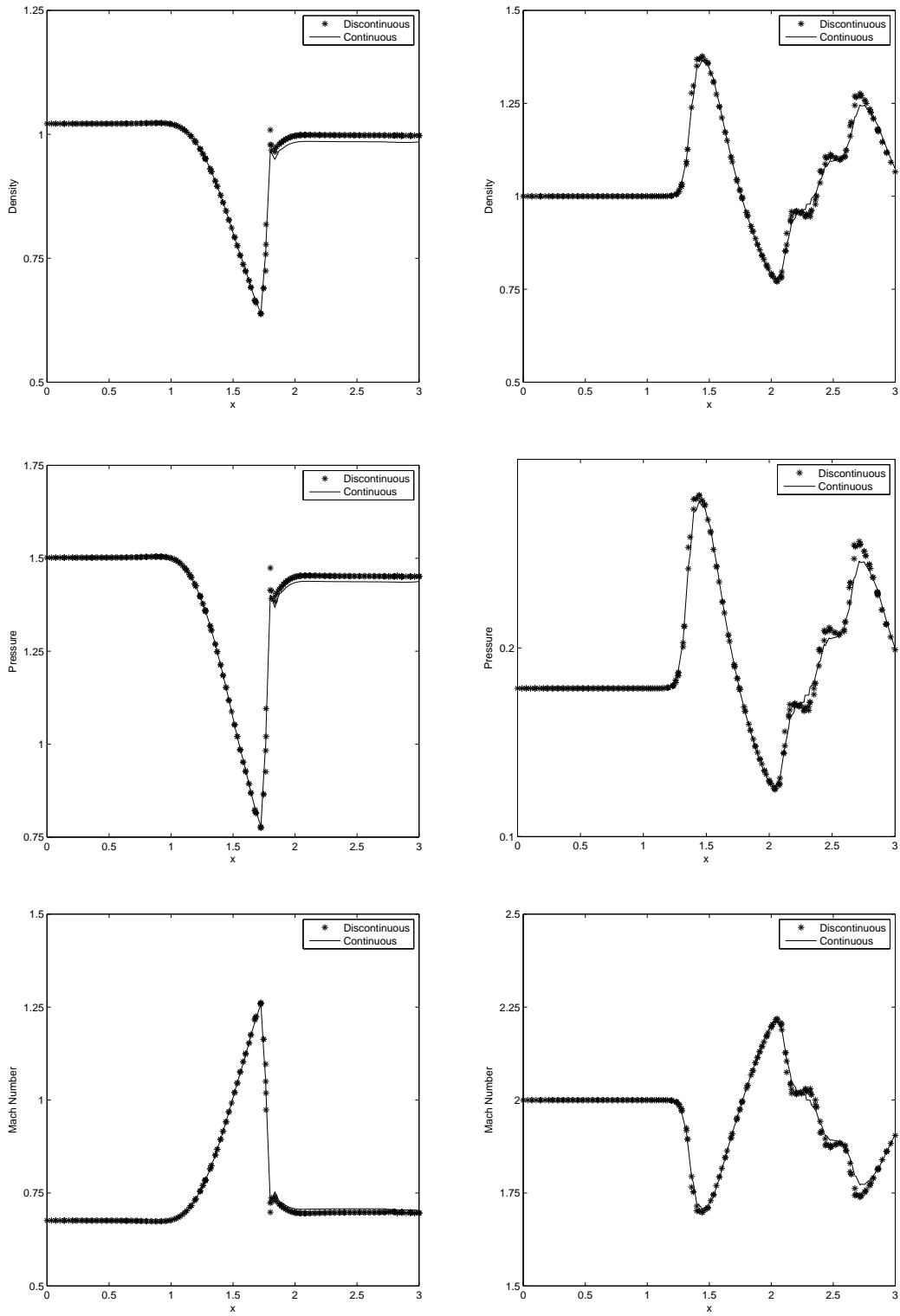


Fig. 12. Comparison of continuous and discontinuous solution profiles along the line $x = 0.2$ for transcritical flow (left) and supercritical flow (right). The variables shown are density (top), pressure (middle) and Mach number (bottom).

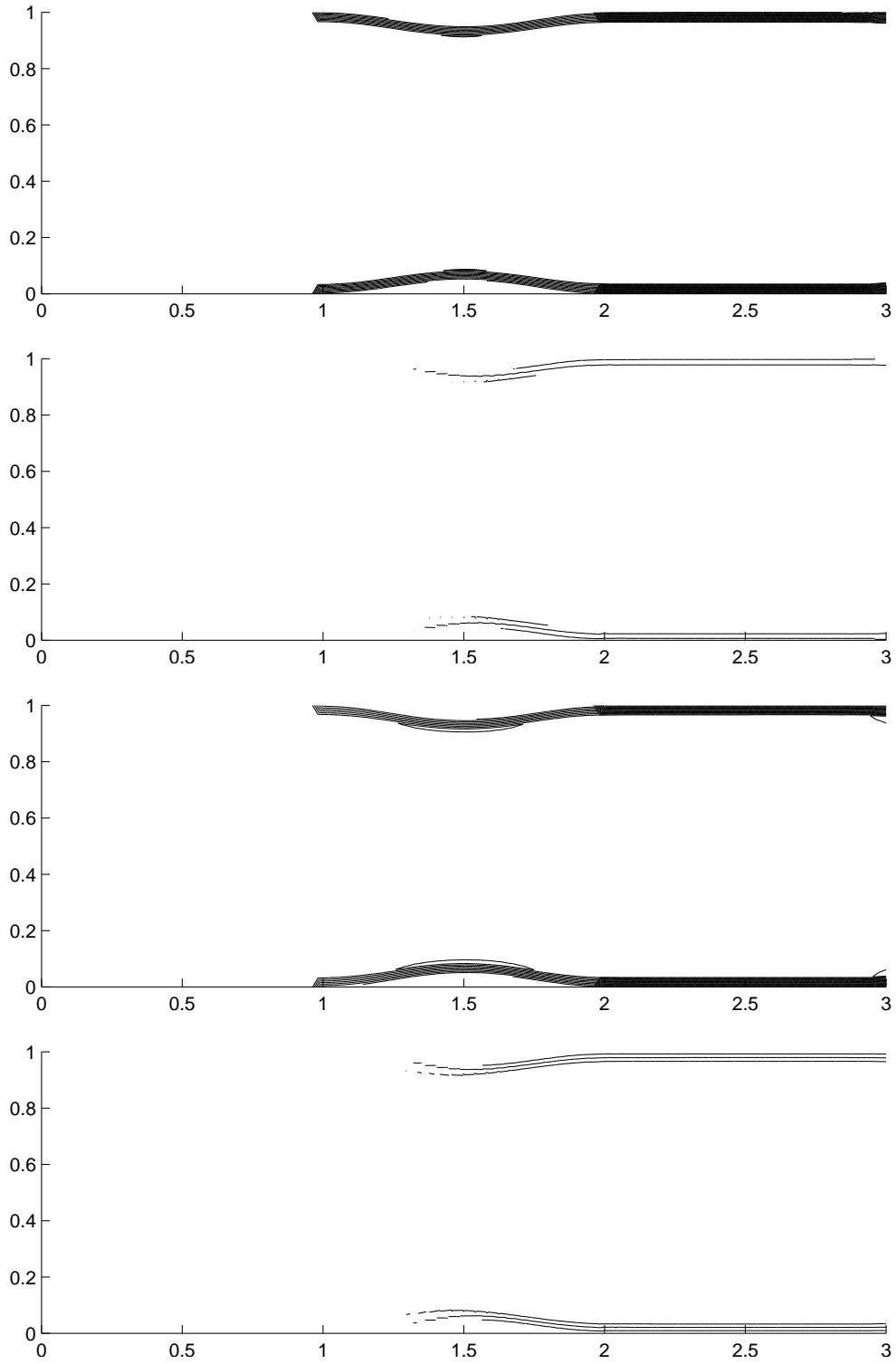


Fig. 13. Contours of entropy deviation for subcritical flow ($M_\infty = 0.5$) through an indented channel for, from top to bottom, the continuous wave decomposition scheme, the discontinuous wave decomposition scheme, the continuous system LDA scheme and the discontinuous system LDA scheme.

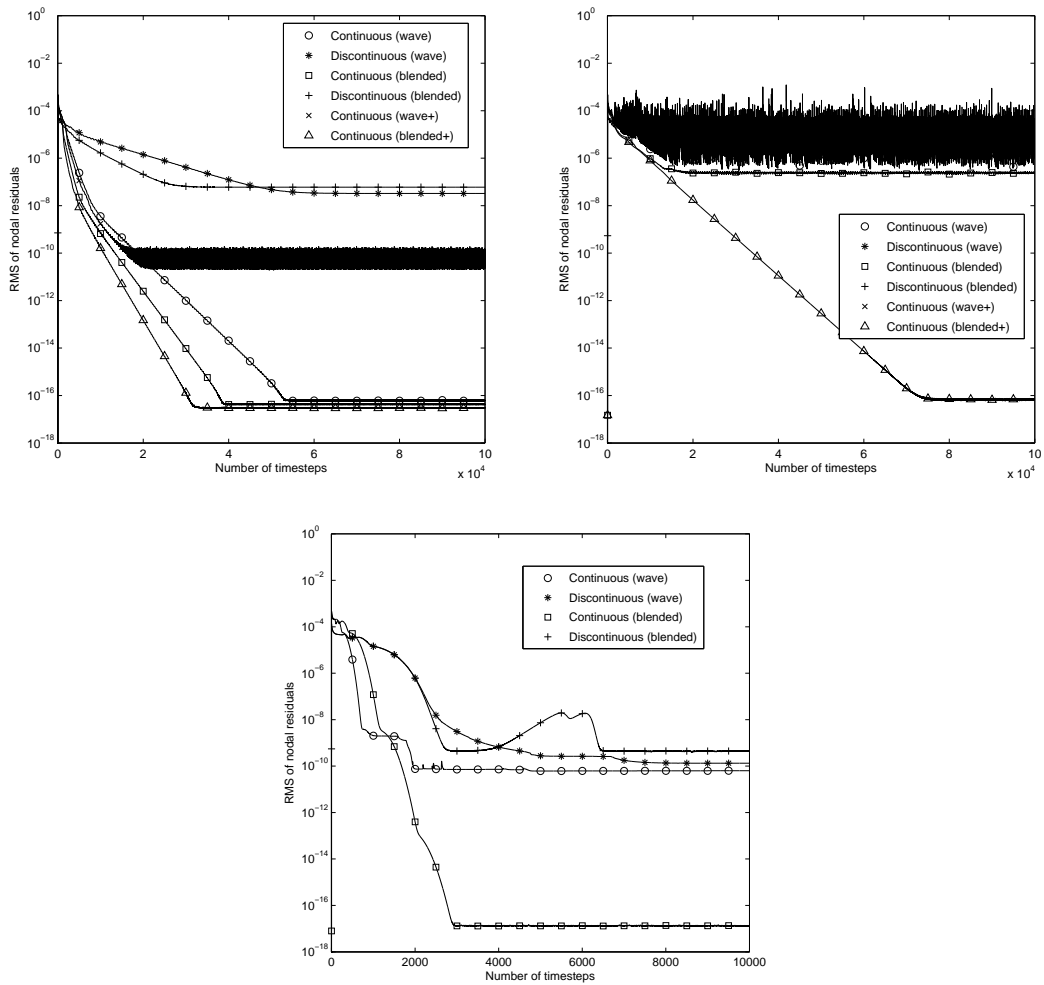


Fig. 14. Convergence histories for the continuous and discontinuous schemes applied to the channel flow test cases with $M_\infty = 0.5$ (top left), $M_\infty = 0.7$ (top right) and $M_\infty = 2.0$ (bottom). The + in the legend indicates that Abgrall's stabilisation term [1] has been applied.

intermediate state. The major contribution to this difference is likely to be associated with the difficulty of representing the discontinuity at the inflow boundary on a computational mesh (in the continuous case it is represented by linear variation across a mesh cell), though it can be reduced by carefully defining intermediate states at inflow, as described in the sixth bullet point below. The convergence histories are not shown here since the magnitudes of the residuals for the discontinuous schemes only drop by about one order of magnitude.

The numerical results achieved for the Euler equations (not all of which are illustrated here) have led to a number of observations.

- The discontinuous scheme tends to exaggerate spurious features seen in the results obtained using the corresponding continuous scheme, *e.g.* small oscil-

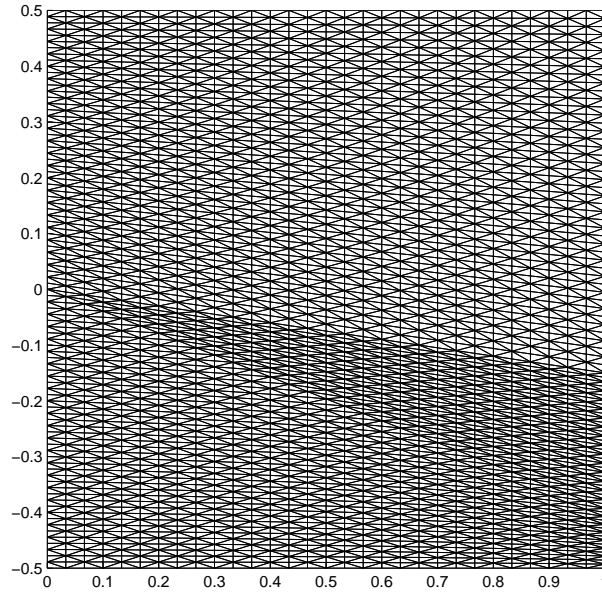


Fig. 15. The 31×91 mesh modified to align mesh edges with the shock and contact discontinuities.

lations caused by the schemes' attempts to capture discontinuities, as seen in Figure 16, are slightly larger in the results obtained using the discontinuous scheme; similarly, in Figure 10, the streamwise oscillations downstream of the shock become more noticeable.

- A shear wave aligned with the edges of the mesh is captured exactly, to machine accuracy by all of the schemes (for both the Euler equations and scalar advection). This property is independent of the method used to distribute the edge fluctuations: it even remains true when a symmetric, central, distribution is used.

This property is actually straightforward to prove. Since the solution is constant within any mesh cell, the contributions to the vertices are always zero. The solution only changes across mesh edges aligned with the discontinuity in the tangential velocity. It is straightforward (though a little tedious) to show that, in the case where the solution is constant on either side of a mesh edge and only the tangential velocity component is different, each component ψ_i in the edge fluctuation (45) is zero and, as a consequence, so are the contributions sent to the cell vertices. This has been verified by the numerical experiments.

- The choice of decomposition and distribution scheme appears to be far less crucial for the edge fluctuations than it does for the cell fluctuations. In particular, the order of accuracy of the overall scheme depends only on the cell fluctuation distribution.
- The convergence of the discontinuous scheme to the steady state tends to stall in the presence of discontinuities in the solution. When they do converge they require more iterations than the continuous schemes, due partly to the more restrictive positivity condition given by (40). This issue will be

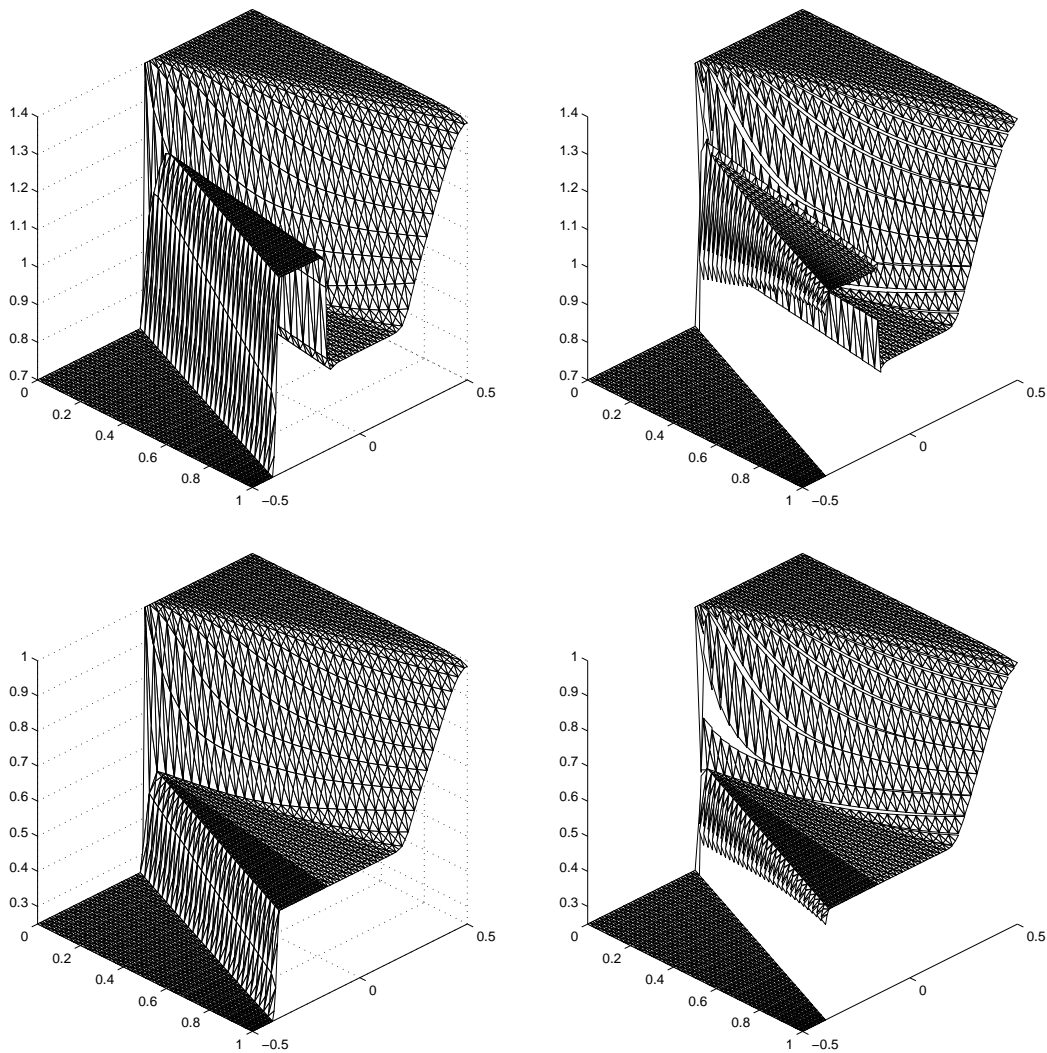


Fig. 16. Surface plots of density (top) and pressure (bottom) for the continuous (left) and discontinuous (right) schemes using the wave decomposition model.

investigated in more depth to ensure that the schemes can be used reliably for the simulation of more complex flow structures than those presented in this paper.

- The scheme is not entropy satisfying so an entropy fix is required to avoid the appearance of expansion shocks in place of rarefaction waves.
- The mesh used to produce the results shown in Figure 16 has four cell-vertices at $(0, 0)$, the point of discontinuity on the inflow boundary and it is not clear how best to define the solution at all of these points. For the results shown, all vertices of cells lying above $y = 0$ were given the first set of values from (59), while all vertices of cells lying below received the second. However, the discontinuities are captured more cleanly if the relevant vertices of the cells which don't have edges on the domain boundary are initialised with the solution values of the intermediate states to which they correspond in the final solution.

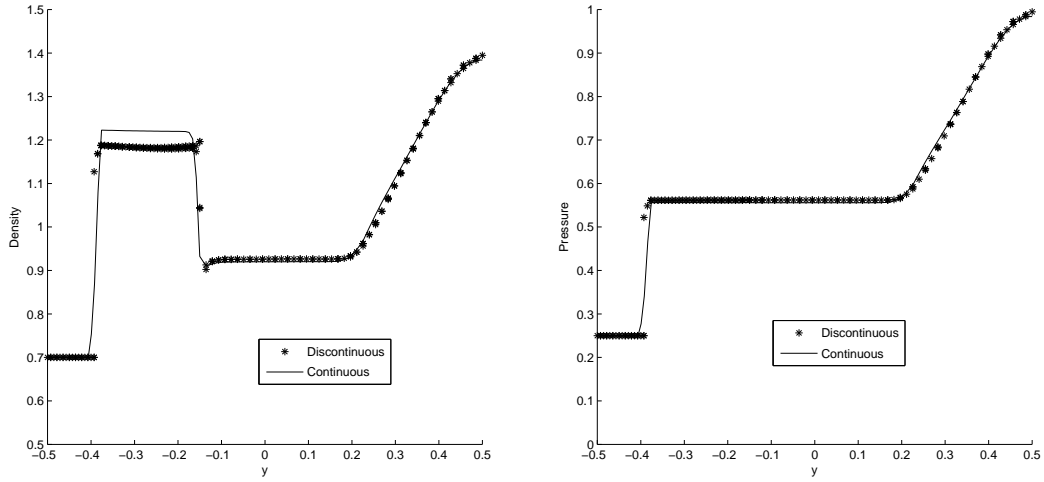


Fig. 17. Comparisons of the density (left) and pressure (right) profiles at outflow for the continuous and discontinuous schemes using the wave decomposition model.

Although this modification could be used to obtain closer agreement between the two density profiles shown in Figure 17, which compares the continuous and discontinuous schemes, it cannot be applied without *a priori* knowledge of the solution. Therefore, it is not used here. However, it is worth noting that the discontinuous fluctuation distribution framework provides a potential solution to this issue, in that it can be used to weakly enforce Dirichlet boundary conditions at inflow by introducing a set of fictitious, exterior, mesh edges around the boundary of the computational domain which can be given the fixed external flow conditions. The boundary conditions would be imposed weakly by distributing the resulting boundary edge fluctuations as described in this paper. Furthermore, the decomposition defined by Equations (41)–(45) can be used to construct the characteristic decomposition typically required for hyperbolic systems. The potential of such an approach will be investigated in future work.

6 Conclusions and Future Work

This work has demonstrated that it is possible to incorporate a discontinuous representation of the dependent variables within the fluctuation distribution framework. It has been successfully applied to linear and nonlinear scalar conservation laws, as well as the Euler equations of gasdynamics. The results presented are on two-dimensional, unstructured, triangular meshes but the algorithm can easily be extended to three space dimensions and to arbitrary polygonal meshes using standard techniques developed for continuous fluctuation distribution. The numerical experiments suggest that approximations obtained using continuous and discontinuous approaches are very similar for smooth flows, and that the new schemes can capture discontinuities exactly

when they are aligned with the mesh edges.

The potential benefits of the proposed framework are wide-ranging since it not only allows discontinuities in the solution and the geometry of the problem to be represented precisely, but also simplifies the process of applying h - and p -refinement techniques and provides a natural framework in which a characteristic decomposition can be applied to weakly enforce Dirichlet boundary conditions.

The aim of this paper was to demonstrate the feasibility of discontinuous fluctuation distribution as a concept. The proposed methods provide a very accurate and robust approach to approximating steady state solutions of scalar hyperbolic conservation laws and have been used to produce high quality approximations to a range of simple, steady state, inviscid compressible flow problems. In terms of their practical use in the simulation of complex flow problems, the schemes are still in the early stages of their development. Some issues demand further investigation, the most pressing being associated with the robustness of the schemes and their convergence to the steady state. At the moment, when a nonlinear system is being approximated and a discontinuity occurs which is not aligned with the mesh, allowing discontinuities in the solution representation tends to exaggerate any downstream oscillations which appear in the continuous approximation. In more complex flow structures than those shown in this paper this can lead to negative pressures and the failure of the method. The mechanism which causes this needs to be understood and rectified, as does the relatively slow convergence of the iteration to the steady state. In both cases, implicit time-stepping may prove to be a valuable tool.

The combination of being relatively expensive when they are applied to the whole computational domain and the likelihood that a discontinuous representation will only provide clear benefits in the representation of specific, localised, situations (*e.g.* discontinuities aligned with the mesh edges, boundary conditions, h - and p -adaptive interfaces) suggests that the discontinuous schemes will be most valuable when applied selectively, alongside a node movement algorithm. A selective algorithm should be straightforward to implement efficiently since the edge- and cell-based fluctuations are treated independently. It is therefore simple to apply a procedure in which edges are flagged if they are to be allowed to be discontinuous and processed separately.

The numerical schemes presented are for steady state problems and provide second order accuracy but the framework is not restricted to these cases.

- The order of accuracy can be improved simply by increasing the order of accuracy of the cell-based distribution, since the discontinuous scheme inherits this accuracy at the steady state. The most natural approach is to

apply the cell subdivision procedure of Abgrall and Roe [5], which could be combined with the technique presented in [16] to remove spurious oscillations. As mentioned above, allowing discontinuities would also simplify the process of adaptively switching the representation of the dependent variable between mesh cells.

- The discontinuous approach can be made time-accurate by applying it on space-time elements [4,9]. Allowing discontinuities in time leads to a form of degenerate double layer scheme (*cf.* [9]), which could potentially allow space-time distribution schemes for which the cell-based distribution does not have to be upwind in time. The discontinuous representation also means that the solution values no longer have to be stored at the mesh nodes: if (in the two-dimensional piecewise linear case) they are instead stored at the midpoints of the mesh edges, it is possible to derive a scheme which is both explicit in time and has a diagonal mass matrix (*cf.* the discontinuous Galerkin method combined with Legendre basis functions). This deserves further investigation since it could lead to a time-dependent scheme which does not require the space-time formulation.

References

- [1] R.Abgrall, Essentially non-oscillatory residual distribution schemes for hyperbolic problems, *J. Comput. Phys.*, **214**:773–808, 2006.
- [2] R.Abgrall, Residual distribution schemes: current status and future trends, *Comput. Fluids*, **35**:641–669, 2006.
- [3] R.Abgrall, T.J.Barth, Residual distribution schemes for conservation laws via adaptive quadrature, *SIAM J. Sci. Comput.*, **24**:732–769, 2002.
- [4] R.Abgrall, M.Mezine, Construction of second order accurate monotone and stable residual distribution schemes for unsteady flow problems, *J. Comput. Phys.*, **188**:16–55, 2003.
- [5] R.Abgrall, P.L.Roe, High order fluctuation schemes on triangular meshes, *J. Sci. Comput.*, **19**:3–36, 2003.
- [6] R.Abgrall, C.-W.Shu, Development of residual distribution schemes for the Discontinuous Galerkin methods: The scalar case with linear elements, *Commun. Comput. Phys.*, **5**:376–390, 2009.
- [7] J.-C.Carette, H.Deconinck, H.Paillère, P.L.Roe, Multidimensional upwinding: Its relation to finite elements, *Int. J. Numer. Meth. Fl.*, **20**:935–955, 1995.
- [8] B.Cockburn, Discontinuous Galerkin methods for convection dominated problems, in *High-Order Methods for Computational Physics*, Barth T.J., Deconinck H. (eds), Springer, pp. 69–224, 1999.

- [9] Á.Csík, H.Deconinck, Space time residual distribution schemes for hyperbolic conservation laws on unstructured linear finite elements, *Int. J. Numer. Meth. Fl.*, **40**:573–581, 2002.
- [10] Á.Csík, M.Ricchiuto, H.Deconinck, A conservative formulation of the multidimensional upwind residual distribution schemes for general nonlinear conservation laws, *J. Comput. Phys.*, **179**:286–312, 2002.
- [11] H.Deconinck, P.L.Roe, R.Struijs, A multidimensional generalization of Roe’s flux difference splitter for the Euler equations, *Comput. Fluids*, **22**(2-3):215–222, 1993.
- [12] H.Deconinck, K.Sermeus, R.Abgrall, Status of multidimensional upwind residual distribution schemes and applications in aeronautics, AIAA paper 2000–2328, 2000.
- [13] H.Deconinck, R.Struijs, G.Bourgois, P.L.Roe, High resolution shock capturing cell vertex advection schemes for unstructured grids, in *Computational Fluid Dynamics*, VKI LS 1994–05, von Karman Institute for Fluid Dynamics, 1994.
- [14] H.M.Glaz and A.B.Wardlow, A high-order Godunov scheme for steady supersonic gas dynamics, *J. Comput. Phys.*, **58**(2):157–187, 1985.
- [15] J.C.C.Henriques, L.M.C.Gato, A multi-dimensional upwind matrix distribution scheme for conservation laws, *Comput. Fluids*, **33**(5-6):755–770, 2004.
- [16] M.E.Hubbard, Non-oscillatory third order fluctuation splitting schemes for steady scalar conservation laws, *J. Comput. Phys.*, **222**:740–768, 2007.
- [17] L.M.Mesaros, P.L.Roe, Multidimensional fluctuation splitting schemes based on decomposition methods, in *12th AIAA CFD Conference Proceedings*, paper AIAA-95-1699, 1995.
- [18] R.-H.Ni, A multiple grid scheme for solving the Euler equations, *AIAA Journal*, **20**:1565–1571, 1981.
- [19] H.Paillère, E.van der Weide, H.Deconinck, Multidimensional upwind methods for inviscid and viscous compressible flows, in *Computational Fluid Dynamics*, VKI LS 1995–02, von Karman Institute for Fluid Dynamics, 1995.
- [20] M.Ricchiuto, R.Abgrall, H.Deconinck, Application of conservative residual distribution schemes to the solution of the shallow water equations on unstructured meshes, *J. Comput. Phys.*, **222**:287–331, 2007.
- [21] M.Ricchiuto, Á.Csík, H.Deconinck, Residual distribution for general time-dependent conservation laws, *J. Comput. Phys.*, **209**:249–289, 2005.
- [22] P.L.Roe, Approximate Riemann solvers, parameter vectors and difference schemes, *J. Comput. Phys.*, **43**(2):357–372, 1981.
- [23] P.L.Roe, Fluctuations and signals, a framework for numerical evolution problems, in *Numerical Methods for Fluid Dynamics*, K.W.Morton, M.J.Baines (eds.), Academic Press, pp. 219–257, 1982.

- [24] P.L.Roe, Upwind differencing schemes for hyperbolic conservation laws with source terms, in *Lecture Notes in Mathematics*, pp. 41–51, 1986.
- [25] P.L.Roe, Linear advection schemes on triangular meshes, CoA Report 8720, Cranfield Institute of Technology, 1987.
- [26] P.L.Roe, L.M.Mesaros, Solving steady mixed conservation laws by elliptic/hyperbolic splitting, in *Proceedings of Fifteenth ICNMF Conference, Monterey*, P.Kutler, J.Flores, J-J.Chattot (Eds.), 1996.
- [27] C.C.L.Sells, Solution of the Euler equations for transonic flow past a lifting aerofoil, RAE TR 80065, 1980.
- [28] R.Struijs, H.Deconinck, P.L.Roe, Fluctuation splitting schemes for the 2D Euler Equations, in *Computational Fluid Dynamics*, VKI LS 1991-01, 1991.
- [29] E.van der Weide, H.Deconinck, Matrix distribution schemes for the system of Euler equations, in *Notes on Numerical Fluid Dynamics*, **57**:113–135, 1997.
- [30] *High Order Discretization Methods*, VKI LS 2006–01, von Karman Institute for Fluid Dynamics, 2006.